Efficient and low-noise single-photon-level frequency conversion interfaces using silicon nanophotonics

Qing Li,[1,2,*] Marcelo Davanço,[1] and Kartik Srinivasan[1,†]

[1] *Center for Nanoscale Science and Technology, National Institute of Standards and Technology, Gaithersburg, MD 20899, USA*
[2] *Maryland NanoCenter, University of Maryland, College Park, MD 20742, USA*

(Dated: February 1, 2022)

Optical frequency conversion has applications ranging from tunable light sources to telecommunications-band interfaces for quantum information science. Here, we demonstrate efficient, low-noise frequency conversion on a nanophotonic chip through four-wave-mixing Bragg scattering in compact (footprint $< 0.5 \times 10^{-4}$ cm^2) Si_3N_4 microring resonators. We investigate three frequency conversion configurations: (1) spectral translation over a few nanometers within the 980 nm band, (2) upconversion from 1550 nm to 980 nm, and (3) downconversion from 980 nm to 1550 nm. With conversion efficiencies ranging from 25 % for the first process to > 60 % for the last two processes, a signal conversion bandwidth > 1 GHz, < 60 mW of continuous-wave pump power needed, and background noise levels between a few fW and a few pW, these devices are suitable for quantum frequency conversion of single photon states from InAs quantum dots. Simulations based on coupled mode equations and the Lugiato-Lefever equation are used to model device performance, and show quantitative agreement with measurements.

arXiv:1510.02527v1 [physics.optics] 8 Oct 2015

Efficient and low-noise frequency conversion has many applications in classical and quantum photonics, for example, casting signals to specific spectral channels for wavelength multiplexing, accessing spectral regions for which high-performance detectors are available, and connecting visible quantum memories with the low-loss telecommunications band. Years of progress in developing frequency conversion technology in both $\chi^{(2)}$ and $\chi^{(3)}$ nonlinear media[1,2], typically based on centimeter long crystals[3] and meter long optical fibers[4], has enabled researchers to demonstrate frequency conversion of quantum states, or quantum frequency conversion (QFC)[5], down to the level of single photon Fock states[6].

Nanophotonic geometries are an attractive way to miniaturize, scale, and customize optical components compared to conventional technology. In particular, microresonators with high quality factor (Q) and small mode volume have proven to be an excellent choice for nonlinear applications by offering small power budget and device size. Nonlinear wave mixing in the silicon platform (including silicon nitride and silicon dioxide) is dominated by the $\chi^{(3)}$ nonlinearity[7], which is also the dominant parametric nonlinearity in optical-fiber-based technology. Most previous $\chi^{(3)}$-based frequency conversion work in nanophotonic devices[8–14] has employed a degenerate or nondegenerate four-wave mixing (FWM) process called parametric amplification (PA), where idler generation goes along with vacuum noise amplification in a system with anomalous dispersion at the pump wavelength. While PA-based frequency conversion works well for many classical applications, it has theoretically been shown that there is a fundamental limit on the achievable signal-to-noise ratio (SNR) for the converted idler at a single-photon-level input, limiting its application for QFC[15]. Alternatively, there is a non-degenerate FWM process, termed four-wave-mixing Bragg scattering (FWM-BS)[16–18], that is typically operated in the normal dispersion regime and does not amplify vacuum fluctuations. As a result, FWM-BS can in principle be a noiseless process, and in fact its Hamiltonian has the form of a state transfer process and can be considered as an active beam splitter[18]. In addition, PA does not allow an arbitrary choice of the target conversion wavelength, which can be important for both the aforementioned classical and quantum applications. In contrast, FWM-BS provides a controllable spectral translation set by the difference in pump frequencies[16,19]. While two earlier works demonstrated FWM-BS in nanophotonic waveguides, the efficiency was $\lesssim 5$ %, despite the use of short pulsed pumps with a peak power of a few Watts[20,21]. Recent theoretical works [22,23] indicate a rising interest in developing FWM-BS using a microresonator structure, in order to achieve efficient single-photon-level frequency conversion with a reasonable power budget.

In this Article, we show for the first time a resonance-enhanced FWM-BS process, using a compact Si_3N_4 microring resonator that significantly reduces the required pump power (< 60 mW continuous-wave pumps). The 1550 nm band and the 980 nm band are considered due to their relevance to low-loss transmission through optical fibers and quantum light generation by InAs/GaAs quantum dots, respectively. We first show efficient (> 25 % conversion efficiency) 980 nm intraband frequency conversion with spectral translation over a few nanometers, which can be used to achieve indistinguishability between InAs/GaAs quantum dots emitting with slightly different wavelengths. Then, we demonstrate wideband frequency conversion from the 1550 nm band to the 980 nm band (upconversion) and the 980 nm band to the 1550 nm band (downconversion), with each showing > 60 % conversion efficiency. The background noise properties for both 980 nm intraband conversion and wideband 980 nm to 1550 nm downconversion are studied using single-photon-level inputs. The performance level of our nanophotonic frequency conversion interfaces (in terms of conversion efficiency and SNR) is comparable to more mature $\chi^{(3)}$ technology such as highly nonlinear and photonic crystal fibers[4,24,25], while operating with much lower power, continuous-wave optical pumps. Moreover, the compact geometry, scalable fabrication process, and versatility make them a promising resource for future applications.

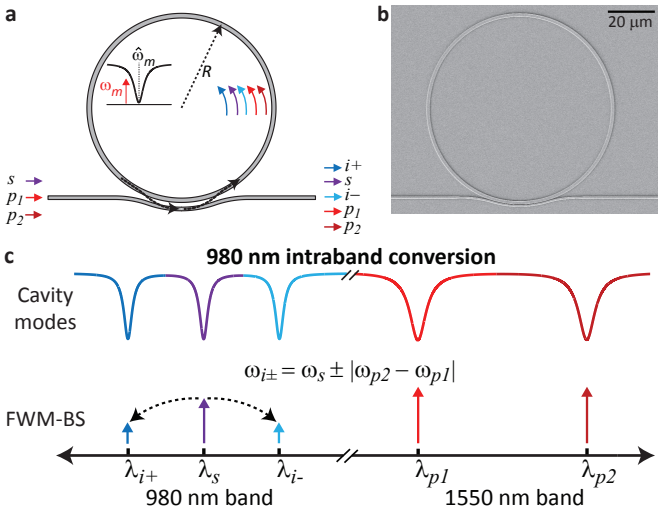


FIG. 1: **Principle of operation and device geometry**. **a**, Schematic of the microresonator geometry used, where an input signal s is converted to idlers $i+$ and $i-$ through application of two pump fields p_1 and p_2. **b**, Scanning electron micrograph of a 40 μm radius microring resonator, showing the pulley-coupled access waveguide. **c**, Schematic of the FWM-BS process for 980 nm intraband frequency conversion, where s, $i+$, and $i-$ are in the 980 nm band and the pumps p_1 and p_2 are in the 1550 nm band. Of critical importance to efficient conversion is the spectral matching of the frequency components generated by FWM-BS ($\omega_{s,i+,i-,p1,p2}$) with the resonant frequencies of the cavity modes ($\hat{\omega}_{s,i+,i-,p1,p2}$). As shown in Figs. 5-6, the same microring can be used to create a frequency conversion interface between the 980 nm and 1550 nm bands.

System Design The silicon nitride (Si_3N_4) platform supports high Q optical modes in the 1550 nm and 980 nm bands together with a relatively large Kerr nonlinearity, both of which are needed for efficient and low power frequency conversion. We use a 40 μm radius microring resonator (Figs. 1a-b) to implement FWM-BS, with the fabrication details provided in the Methods. The first FWM-BS scheme under study is illustrated in Fig. 1c, where the interference of two 1550 nm band pumps effectively creates a grating in the Si_3N_4 $\chi^{(3)}$ nonlinear medium that scatters the 980 nm input signal to two idlers, which are separated from the signal by an amount equal to the difference in pump frequencies. These two idlers are labeled as $i-$ and $i+$ ($i+$ denotes the idler with higher frequency), similar to the Stokes and anti-Stokes sidebands in Raman scattering. In whispering-galley-mode geometries, phase matching is satisfied by the correct choice of azimuthal mode numbers, while energy conservation has to be met through careful engineering. The conversion efficiencies for $i\pm$ are a function of their frequency detunings with respect to their corresponding cavity modes, which can be derived as $\delta\hat{\omega}_{\pm} \approx (\hat{\omega}_{i\pm} - \hat{\omega}_s) \mp |\hat{\omega}_{p1} - \hat{\omega}_{p2}|$ (see Supplementary Section I.A), where $\hat{\omega}_{p1,p2,s,i\pm}$ denotes the resonance frequency accommodating the pump 1, pump 2, the signal s, and idler $i_{\pm}$, respectively. The resonance frequencies in each band can be approximated by the Taylor series $\hat{\omega}_\mu = \hat{\omega}_0 + D_1\mu + \frac{1}{2}D_2\mu^2 + \frac{1}{6}D_3\mu^3...$, where $\hat{\omega}_0$ is the reference frequency, $D_1/2\pi$ is the free spectral range (FSR) of the resonator at $\hat{\omega}_0$, D_n $(n = 2,,3...)$ are parameters characterizing the resonance dispersion, and μ is an integer representing the relative mode order number with respect to $\hat{\omega}_0$. As a result, the frequency detuning for $i\pm$ corresponding to pump separation of $|\mu|$ FSRs is given by $\delta\hat{\omega}_{\pm|\mu|} \approx \pm\delta D_1|\mu| + \frac{1}{2}\delta D_{2,\mp}\mu^2...$, where $\delta D_1 \equiv D_1^{980} - D_1^{1550}$ and $\delta D_{2,\pm} \equiv D_2^{980} \pm D_2^{1550}$, with the 980 and 1550 superscripts marking the reference wavelengths in the 980 nm and 1550 nm bands, respectively. The first order frequency matching condition (i.e., $\delta D_1 \approx 0$) is satisfied by using a ring waveguide geometry that exhibits $n_g^{1550} = n_g^{980}$ (Fig. 2a), where n_g stands for the group index and is inversely proportional to the FSR. Moreover, it is important to be in the overcoupled regime for the 980 nm band to extract the generated idlers efficiently while maintaining a reasonably high Q in the 1550 nm band for resonance enhancement. The conventional point coupling, which relies upon the evanescent field overlap between the modes of a straight waveguide and the resonator, presents difficulty in doing so since the coupling becomes significantly weaker at shorter wavelengths (Fig. 2b). This problem is solved here by implementing the pulley coupling scheme[26–28], which has an increased interaction length (Fig. 1b) and thus the coupling Q depends on both the evanescent field overlap and phase matching. Because the resonant modes in the 1550 nm band extend further outside the ring core than in the 980 nm band, resulting in larger mode overlap, we choose an access waveguide width that is phase matched (mismatched) to the resonant modes in the 980 nm (1550 nm) band, resulting in similar Q values in the two bands. This is demonstrated by the simulation result in Fig. 2b, and confirmed by linear transmission measurements of the fabricated devices. By varying the coupling parameters (gap and coupling length) across multiple devices, we find a device operating in the overcoupled regime in both the 1550 nm and 980 nm bands, with loaded Q values $\approx 1.5 \times 10^5$ (linewidth $\kappa/2\pi \approx 1.29$ GHz) and 2.4×10^5 ($\kappa/2\pi \approx 1.28$ GHz), respectively (Fig. 2c-d). In addition, with the aid of a 200 MHz resolution wavemeter, the resonances in each band can be measured (Fig. 2e-f), from which we extract $D_1^{1550}/2\pi = 572.39$ GHz $\pm$ 0.05 GHz and $D_1^{980}/2\pi = 572.25$ GHz $\pm$ 0.05 GHz, where the uncertainty is due to the wavemeter resolution and represents a one standard deviation value. The difference in FSR between the 1550 nm and 980 nm bands is well below the resonator linewidth, indicating the first order frequency matching condition has been satisfied. We also extract high-order dispersion terms D_2 and D_3 in the two wavelength bands of interest and find that the resonator shows normal dispersion ($D_2 < 0$) in both bands. In general, D_2 and D_3 need to be taken into account for the frequency detuning calculation of idlers when the two pumps are widely separated, as the deviation of resonance frequencies from an equally spaced frequency grid (separated by one FSR) becomes comparable to the resonance linewidth for large $|\mu|$ values.

980 **nm intraband conversion.** The experimental setup is shown in Fig. 3a, where the two 1550 nm pumps are amplified and combined with the 980 nm signal, and coupled to the chip using a lensed fiber (coupling loss $\approx$ 5.5 dB and 6.5 dB per facet for the 1550 nm and 980 nm band, respectively).

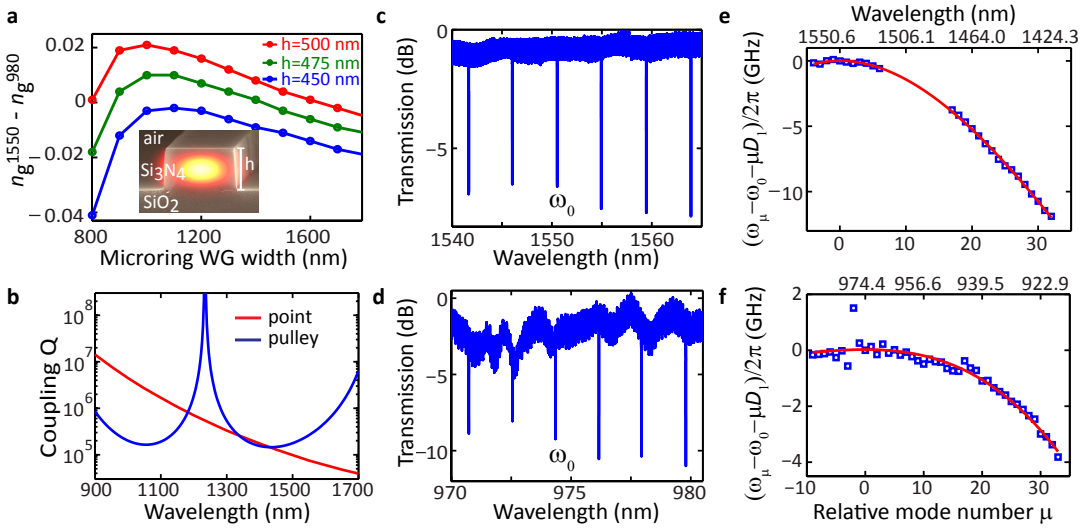


FIG. 2: **Device design, dispersion, and coupling characterization**. **a**, Simulated group index difference between the 1550 nm and 980 nm bands for various Si_3N_4 waveguide cross-sections with top air cladding and bottom oxide cladding (inset), from which a 1400 nm $\times$ 480 nm ring waveguide cross-section is chosen for this work. **b**, Simulated coupling Q for a 820 nm wide waveguide coupling to the microring with gap of 250 nm, considering both point coupling and pulley coupling with a coupling length of 25 μm. **c-d**, Linear transmission scan of the fabricated sample for the 1550 nm and 980 nm bands, with intrinsic/total quality factors measured to be $\approx 4.5\times10^5/1.5\times10^5$ and $9.0\times10^5/2.4\times10^5$, respectively. **e-f**, Deviation of the measured resonance frequencies (markers) from an equidistant frequency grid $\omega_0+\mu D_1$ for the 1550 nm and 980 nm bands, where $D_1^{1550}/2\pi = 572.39$ GHz $\pm$ 0.05 GHz and $D_1^{980}/2\pi = 572.25$ GHz $\pm$ 0.05 GHz (the uncertainty is due to the wavelength resolution and represents a one standard deviation value). The solid lines are the fitting curves using dispersion parameters $D_2/2\pi \approx -31.04$ MHz and $D_3/2\pi \approx 0.71$ MHz for the 1550 nm band, and $D_2/2\pi \approx -3.43$ MHz and $D_3/2\pi \approx -0.30$ MHz for the 980 nm band.

To tune both pump lasers into resonance, narrowband filters (bandwidth $\approx$ 1 nm) are placed in front of each 1550 nm detector to select each pump while it scans across its resonance with decreasing frequency detuning, showing a characteristic triangular resonance shape from a combined Kerr-nonlinear and thermal resonance shift[29]. As we reduce the spectral distance between one pump and its nearby resonance, the intracavity power rises and the dominant thermal shift sends all the resonances towards lower frequencies, effectively increasing the spectral distance of the other pump laser with respect to its accommodating resonance. Therefore, it is necessary to tune the two pump lasers in an interactive and iterative way until both are thermally locked on their respective resonances.

Once the pumps are thermally locked, we characterize the frequency conversion process through two types of measurements. The first is to spectrally resolve the light exiting the chip using an optical spectrum analyzer (OSA). The second is to examine signal depletion and idler generation by swept wavelength spectroscopy of the signal resonance. Figure 3b shows the experimental results when the two pumps are separated by one FSR and of nearly equal power. When the pump power is low (first column, case I), only two small sidebands ($i+$ and $i-$) are observed in the 980 nm spectrum (second column, case I); as the pump power increases (case II), secondary pump peaks appear in the 1550 nm spectrum from pump mixing, which in turn generate higher-order idlers in the 980 nm spectrum. The on-chip conversion efficiency, defined as the converted idler photon flux at the waveguide output divided by the input signal photon flux at the waveguide input, reaches a maximum of -6.2 dB for both $i+$ and $i-$ at 16 mW power per pump (case III). In addition, multiple high-order idlers are generated, though the red idlers decrease more rapidly than the blue ones due to an accidental mode shift of the 978 nm resonance (Fig. 2f, $\mu = -2$) caused by mode interactions (see Supplementary Section III). If we further increase the pump power (case IV), more sidebands are observed in both the 1550 nm and 980 nm bands, but the conversion efficiency for $i+$ and $i-$ slightly decreases, indicating there is a saturation level for a specific idler. The OSA data is complemented by transmission measurements in the 980 nm band (third column). First, we use a narrowband filter (centered on the signal resonance with bandwidth $\approx$ 0.4 nm) to reject all of the generated idlers and provide a measurement of the signal transmission. As the pump power increases, the signal resonance evolves from overcoupled (cases I and II) to critically coupled (case III) and then undercoupled (case IV), indicating an increased intrinsic loss that is attributed to signal depletion due to the frequency conversion process. In addition, mode splitting starts to appear as the pump power increases, a phenomenon expected when there is a strong coupling between the signal and adjacent idlers (see next section and also Supplementary Section I.A). Next, we remove the narrowband filter and directly detect light in the whole 980 nm band. At low pump powers (cases I and II), the transmission scan is the same as the linear case, but when the conversion efficiency is high (cases III and IV), the extinction ratio becomes much smaller, suggesting a significant amount of idler generation when the signal is on-resonance. Moreover, mode splitting

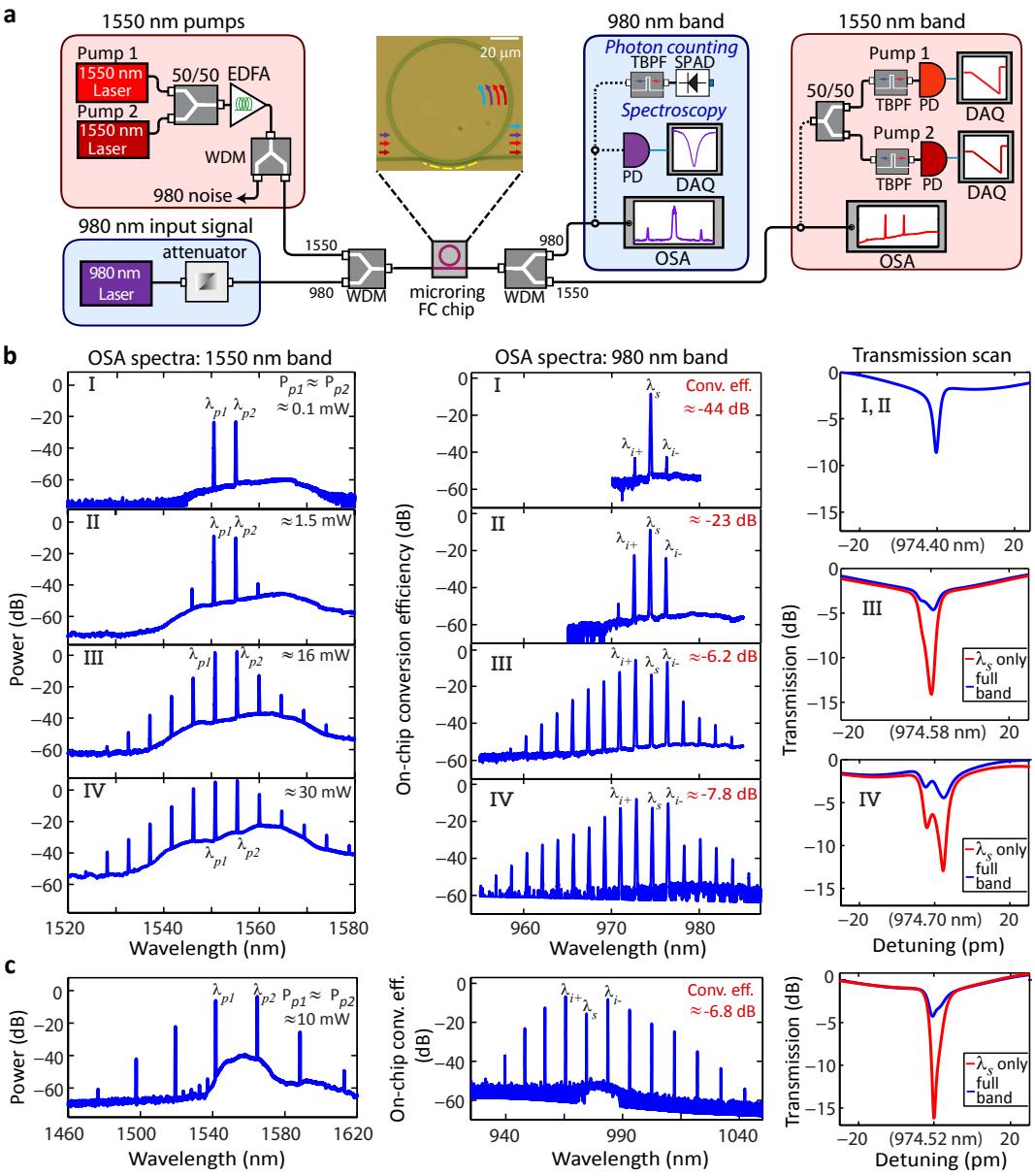


FIG. 3: 980 **nm intraband frequency conversion**. **a**, Experimental setup for the 980 nm intraband frequency conversion: EDFA, erbium-doped fiber amplifier; WDM: wavelength-division multiplexer; TBPF: tunable bandpass filter; SPAD: single-photon avalanche diode; PD: photodetector; DAQ: data acquisition; OSA: optical spectrum analyzer. **b**, Experimental frequency conversion results for two pumps separated by one free spectral range (FSR). The two pumps and the signal are located at 1550.6 nm, 1555.2 nm, and 974.4 nm, respectively. Four cases (I-IV) corresponding to different pump power levels are displayed: the first two columns correspond to the OSA spectra in the 1550 nm and 980 nm band, respectively, and the last column shows the transmission scans of the signal around its thermally shifted resonance (x axis origin). The transmission scan data is taken both with a narrowband filter centered on the signal resonance (rejecting all converted idlers), and across the full 980 nm band (no narrowband filter). In the transmission scan data for cases I and II, these two curves are identical. **c**, Experimental results for the two pumps separated by five FSRs. The two pumps are located at 1541.5 nm and 1564.5 nm and the signal is the same as the one FSR case (974.4 nm). In the 1550 nm band OSA spectra in **b**-**c**, a power of 0 dB is referenced to 1 mW.

is also evident at sufficiently high powers (case IV). We can also increase the separation between the two pumps. When they are separated by 5 FSRs (Fig. 3c), the optimum on-chip conversion efficiency for $i+$ and $i-$ is similar to the 1 FSR case, indicating the phase matching condition is well satisfied. Thus, in this configuration, frequency conversion with a signal translation as low as 1.8 nm (1 FSR) and as large as 9.0 nm (5 FSR) can be achieved with an efficiency as high as 25 % in each first-order idler.

Numerical simulations Four-wave mixing in $\chi^{(3)}$ resonators can be described by the Lugiato-Lefever equation (LLE), a version of the nonlinear Schrodinger equation that includes

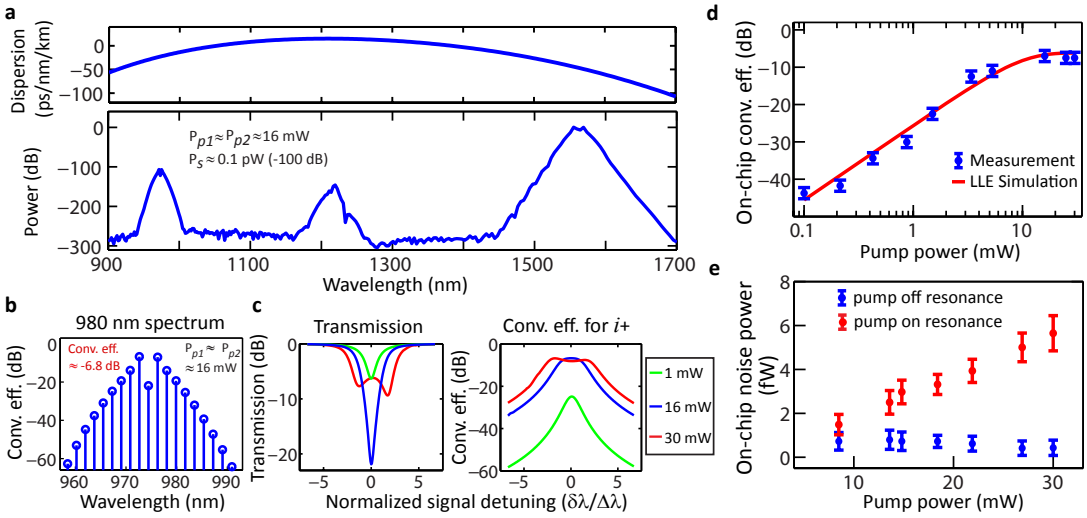


FIG. 4: **Numerical simulations and SNR measurement for 980 nm intraband conversion. a**, (Bottom) Simulated optical spectrum at the output of the waveguide based on a modified Lugiato-Lefever equation for the pump power of 16 mW per pump and signal power of 0.1 pW. (Top) Plot of the dispersion parameter, obtained from an eigenfrequency mode solver for the micresonator under study and converted to an equivalent group velocity dispersion. **b**, zoomed-in 980 nm spectrum with the y axis normalized to the photon flux of the input signal. **c**, Simulated transmission scan of the signal resonance (left) and the on-chip conversion efficiency for $i+$ (right) for several different pump powers using the modified LLE method. The x axis is the wavelength detuning normalized by the linewidth of the resonance ($2\Delta\lambda \approx 4$ pm). In both **a** and **c**, a power of 0 dB is referenced to 1 mW. **d** Measured (blue markers) and simulated (red line) conversion efficiency of $i+$ as a function of pump power. **e**, Measured on-chip background noise at $i+$ frequency with ≈ 120 GHz detection bandwidth for various pump powers with the pumps off- and on-resonance with their respective cavity modes. The error bars in **d** and **e** are due to fluctuations in the detected signal by the SPAD, and represent a one standard deviation value. In all of the above, the 1550 nm pump separation is 1 FSR.

driving and dissipation and which has been successfully applied to study microcavity frequency combs[30]. To understand our experimental results, numerical simulations based on a modified form of the conventional LLE formalism are carried out. The modification is needed for FWM-BS to allow for three independent inputs (i.e., two pumps and one signal). In addition, coupled mode equations are also used[31,32]. Though the two approaches are essentially equivalent[33,34], they differ in detailed forms and numerical implementation, which may render one better than the other depending on the scope of the problem. For example, the coupled mode equations are usually preferred for revealing the underlying physics, while the LLE method is capable of capturing all relevant physical mechanisms by automatically including a complete set of modes into simulation.

Figure 4a shows the simulation results based on the modified LLE method (see Methods) for the case of 16 mW power per pump. Compared to the corresponding experimental results (Fig. 3b case III), we find the modified LLE simulation successfully models the pump mixing in the 1550 nm band and the multiple idler generation in the 980 nm band (Fig. 4b). In addition, there is a small noise band in the anomalous dispersion region (1100 nm to 1300 nm), which arises from modulation instability processes (i.e., one photon from the 980 nm signal and one photon from the 1550 nm pumps are converted to nearly degenerate photon pairs near the wavelength of 1200 nm), though such processes are generally frequency-mismatched and small enough to be neglected. The transmission scan of the signal resonance from the LLE simulation (Fig. 4c, left) also shows good agreement with the experimental data, and the observed mode splitting is explained by a simplified set of coupled mode equations to result from strong couplings induced by FWM-BS between the signal and its adjacent idlers (Supplementary Section I.A). Generally, increasing pump powers leads to larger mode splitting and increased conversion bandwidth for the signal photon (Fig. 4c, right), but not necessarily higher conversion efficiency for a specific idler as its conversion efficiency will eventually saturate.

SNR measurement Along with conversion efficiency, a key metric for quantum photonic applications (as well as some classical applications) is the background noise generated in the converted idler band. In general, one may expect that noise to originate due to the presence of strong pump fields, which through processes such as Raman scattering, may generate photons that are either directly resonant with the converted idler, or are resonant with the input signal and get frequency converted together with it. One advantage of the scheme presented here is that the signal and idler are about 600 nm away from the strong pump fields (and are on their anti-Stokes side), suggesting that noise due to Raman scattering should be limited.

To determine the suitability of this system as a QFC interface, we consider the conversion efficiency and SNR for an input signal at the single photon level (≈ 1 pW, corresponding to photon flux $\approx 5 \times 10^6$ s^{-1}, which is consistent with the photon flux produced by systems such as a quantum dot single

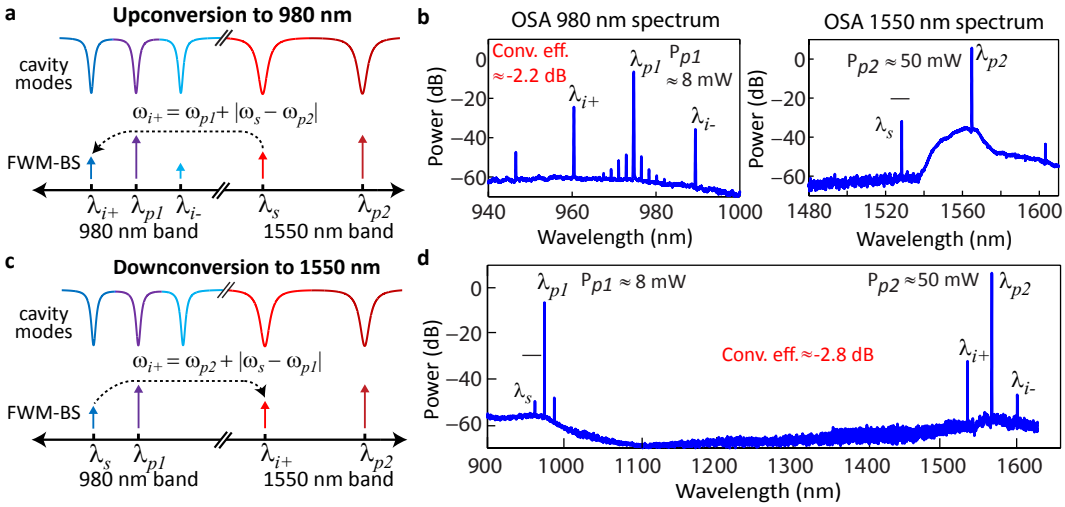


FIG. 5: **Wideband frequency conversion interface to the telecommunications band**. **a**, Schematic of the signal upconversion from the 1550 nm band to the 980 nm band. **b**, Representative experimental result for upconversion: the two pumps and the signal are located at 974.4 nm, 1564.5 nm and 1528.0 nm, respectively. The small horizontal bar above the signal indicates its input power. In the 980 nm spectrum, other than $i+$ and $i-$ and a group of small idlers near the 980 pump which correspond to the upconverted ASE noise of the EDFA, there is another small peak near 946.2 nm due to the mixing between $i+$ and the 980 nm pump. Similarly, in the 1550 nm spectrum the small peak near 1602.8 nm is due to the the mixing of the signal and the 1550 nm pump. **c**, Schematic of the signal downconversion from the 980 nm band to the 1550 nm band. **d**, Representative experimental result of downconversion showing a full spectrum: the two pumps and the signal are located at 974.4 nm, 1559.8 nm, and 961.9 nm, respectively. The small horizontal bar above the signal indicates its input power. In **b** and **d**, a power of 0 dB is referenced to 1 mW.

photon source[35] triggered at 50 MHz and with a source efficiency of 10 %). A single-photon avalanche diode (SPAD) is used to measure the power in the converted idler band, which is spectrally isolated from the 1550 nm pumps using a WDM and a 0.4 nm bandwidth bandpass filter (Fig. 3a). The on-chip conversion efficiency, background noise power, and SNR are determined from knowledge of the coupling loss and insertion losses of the filtering elements. As shown in Fig. 4d, the on-chip conversion efficiency as a function of pump power for the $i+$ idler agrees with the LLE simulation, and peaks at ≈ 25 %. We next measure the noise power by turning off the input signal and considering two cases, when the pumps are on-resonance with their respective cavity modes and when they are off-resonance (Fig. 4e). Off resonance, any measured noise is found to be broadband emission from the erbium-doped fiber amplifier (EDFA) used for the pump, and can be significantly reduced by filtering at the input side, prior to the chip (see Fig. 3a, WDM filter placed after the EDFA). On resonance, we observe noise above the EDFA-determined background, at the level of a few fW. This noise is mainly contributed by the Si_3N_4 microresonator, though its origin is still under investigation (see Supplementary Section VI). At the optimum conversion efficiency (25 % at pump power ≈ 16 mW), the SNR is larger than 80 : 1 for the aforementioned input signal photon flux $\approx 5 \times 10^6$ s^{-1}. Moreover, for triggered sources, we only need to consider generated noise that temporally coincides with the single photon emission, which is produced at well defined times (the triggering times) and over well defined intervals (the spontaneous emission lifetime; typically ≈ 1 ns for an InAs/GaAs quantum dot[35]). Therefore, either gated detection or temporal gating of the signal via amplitude modulation[36] can be used, with a typical duty cycle of 5 % (for a 50 MHz triggering rate). Since the measured background noise comes from a continuous-wave pump, we expect the corresponding noise level in the gated case to be reduced by a factor equal to the duty cycle, which will push the SNR to $> 1000 : 1$ at the optimum conversion efficiency.

Telecommunications band frequency conversion interface
In addition to frequency conversion within the 980 nm band, we can use the same device for frequency conversion between the 1550 nm and 980 nm bands. As illustrated by Figs. 5a and 5c, with one pump in each band, the signal can be upconverted (downconverted) from the 1550 nm (980 nm) band to the 980 nm (1550 nm) band. Although the pump power available from our 980 nm laser is limited (maximum ≈ 8 mW), it can be compensated by using a relatively strong pump in the 1550 nm band, since the conversion efficiency is determined by the product of the two pump powers[17]. Figure 5b shows one example of upconversion, measured using the experimental setup shown in Fig. S6 of the Supplementary, where the signal is separated from the 1550 nm pump by 8 FSRs (i.e., $\mu = 8$). In the 980 nm band spectrum, the converted blue idler ($i+$) shows a conversion efficiency ≈ -2.2 dB while the red idler ($i-$) is much weaker (as in the 980 nm intra-band case, we define conversion efficiency in terms of photon flux). The difference in the conversion efficiency indicates different frequency detunings for the two idlers, which is expected as high-order dispersion terms become important when $|\mu|$ is large (see Supplementary Section IV for more detailed discussions). In addition, we find the amplified spontaneous

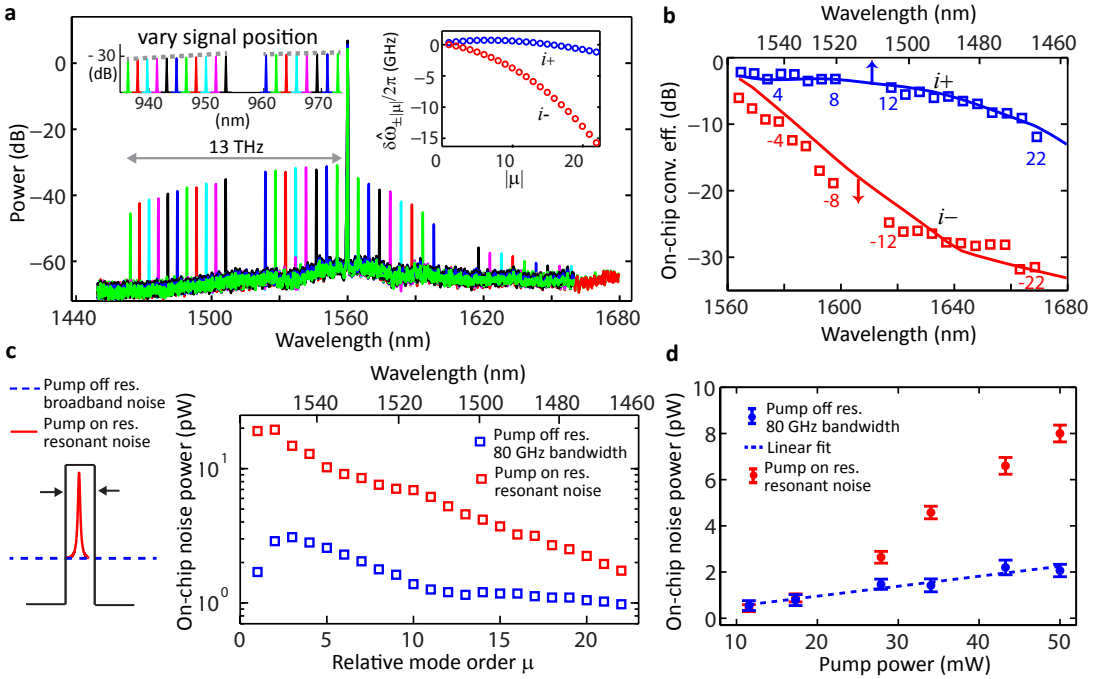


FIG. 6: **Wideband frequency downconversion bandwidth and background noise measurement.**. **a** Superimposed OSA spectra in the 1550 nm band for different signal separation from the 980 nm pump with fixed pump powers in the 1550 nm and 980nm bands (50 mW and 8 mW, respectively). The inset on the left side illustrates the position of the signal input from 980 nm band lasers covering wavelength ranges of 930 nm to 955 nm and 960 nm to 990 nm. In addition, the input signal power decreases as it goes to shorter wavelengths, which also contributes to the reduced idler power as observed in the 1550 nm spectrum. For both the main figure and its left inset, a power of 0 dB is referenced to 1 mW. The inset on the right side shows the calculated frequency detuning for $i+$ and $i-$ at different idler positions. **b** Measured (markers) and simulated (solid lines) conversion efficiencies for $i+$ and $i-$ as a function of the signal separation from the 980 nm pump. **c**-**d**, Measured on-chip background noise power with a 80 GHz detection bandwidth for the pump-off-resonance and the resonant noise for $i+$ when the pump is on-resonance for **c**: different idler positions while keeping the 1550 nm pump power fixed at 50 mW and for **d**: fixed idler position ($\mu = 7$) while varying the 1550 nm pump power. The error bars in **d** are due to fluctuations in the SPAD detection rate, and represent a one standard deviation value. The error bars in **c** are smaller than the marker size.

emission (ASE) around the 1550 nm pump (largely due to the EDFA) is also upconverted to the 980 nm band (small peaks around the 980 nm pump). By adding a narrowband filter after the EDFA, the ASE of the 1550 nm pump can be suppressed.

As one would expect, if efficient 1550 nm to 980 nm upconversion can be achieved in this system, efficient 980 nm to 1550 nm downconversion should also be achievable, and easily measured by simply moving the input signal to the 980 nm band (Fig. 5c). Figure 5d shows a representative downconversion spectrum when the separation between the input signal and the 980 nm band pump is 7 FSRs ($\mu = 7$), where in this case a narrowband ASE rejection filter surrounding the 1550 nm pump is applied (see Supplementary Fig. S7a). Along with a conversion efficiency for $i+$ that is similar to the upconversion case (≈ -2.8 dB), we see the ASE rejection filter has successfully suppressed the spurious peaks present in the upconversion spectrum.

To further explore the properties of wideband frequency conversion based on the FWM-BS scheme, we focus on the downconversion case by varying the signal position in the 980 nm band while keeping pump powers in the 1550 nm and 980 nm band $\approx$ 50 mW and 8 mW, respectively (Fig. 6a). As we increase the separation between the signal and the 980 nm pump (i.e., μ increases), the blue idler $i+$ moves away from the 1550 nm pump by an equal amount of frequency shift with slowly decreasing power. By contrast, the red idler $i-$ shows slightly worse conversion efficiency than $i+$ when μ is small, but as μ increases its power decreases much more rapidly. Their different performance can be understood by calculating the corresponding frequency detunings (Fig. 6a inset, right), which reveal that $i+$ has a small frequency detuning for up to 22 FSR separation from the 1550 pump, while the frequency detuning for $i-$ is already comparable to the resonance linewidth after 5 FSRs. In Fig. 6b, the conversion efficiencies for both $i+$ and $i-$ are extracted from Fig. 6a (markers), and agree with the simulation results based on coupled mode equations (solid lines, see Supplementary Section I.B). With less than 60 mW total pump power, the maximum conversion efficiency for $i+$ is measured to be $\approx$ 60 % (-2.2 dB), and the spectral range over which the input signal can be tuned without reducing the conversion efficiency by more than 3 dB (i.e., conversion efficiency > 30 %) is estimated to be nearly 8.2 THz. Even when the signal is 13 THz away from the 980 nm pump, the conversion efficiency for $i+$ is still more than 10 %.

To measure the SNR level for the wideband frequency con-

version (see Supplementary Section V), we turn off the signal and measure the noise at the idler frequency while keeping the pumps on. Narrowband filters are added at the input side for each pump to suppress its ASE level so that the single-photon-level signal and idlers are not overwhelmed by the ASE noise. For the upconversion case as shown in Fig. 5a, the 1550 nm pump is expected to generate little noise in the 980 nm band as already demonstrated in the 980 nm intraband frequency conversion (Fig. 4e), although it is not trivial to suppress the 980 nm pump to sub pW level on the detection side ($>$ 100 dB suppression) so that single-photon-level noise can be measured. For the downconversion case, the noise is found to be mostly from the 1550 nm pump and the contribution of the 980 nm pump is negligible. At the output, after filtering out the 1550 nm pump, the transmitted light goes through a narrowband filter with a tunable bandwidth (32 pm to 600 pm) and center wavelength (1460 nm to 1560 nm) before detection by a SPAD. When the 1550 nm pump is off-resonance, the noise power scales with the filtering bandwidth and exhibits a smooth spectral response as we shift the center wavelength of the filter, indicating it is a broadband noise. On the other hand, when we tune the pump into resonance, the detected noise initially stays the same if the narrowband filter is out of resonance, but increases significantly if the filter is centered on the idler resonance. The increased noise power changes little as we adjust the filtering bandwidth, suggesting this portion of noise is resonant. Figure 6c shows the measured on-chip noise power for idlers with different spectral separation from the 1550 nm pump (power fixed $\approx$ 50 mW). The pump-off-resonance noise is identified as anti-Stokes Raman scattering generated inside fiber after the EDFA, as the noise is almost the same if we remove the chip and introduce a similar insertion loss between two lensed fibers (see Supplementary Section VI for more details). On the other hand, the resonant noise (i.e., noise generated at the idler frequency with bandwidth limited by the cavity linewidth) for the pump-on-resonance case is believed to be from the Si_3N_4 microresonator, and decreases rapidly as the idler moves away from the pump. For example, the resonant noise is measured to be $\approx$ 8 pW for the $\mu = 7$ idler (1528 nm resonance). Assuming the input signal is from a single photon emitter with a photon flux $\approx 5 \times 10^6$ s^{-1} ($\approx$ 1 pW power), the converted blue idler has a power $\approx$ 0.52 pW (≈ -2.8 dB conversion efficiency). At first glance, it seems the signal will be overwhelmed by the noise. However, just as we discussed in the intraband conversion case, for a triggered single photon source, either gated detection or temporal gating of the light exiting the frequency conversion device can be used, with a typical duty cycle of 5 %. This will improve the SNR to be more than unity under current conditions. Another straightforward route to reducing the noise power is to design a frequency-matched idler that has a larger spectral separation from the pump. Improving the Si_3N_4 material quality may also be important, as the resonant noise is suspected to be correlated with the significant material absorption inferred by a relatively large thermo-optic shift for the pump modes in the 1550 nm band (see Supplementary Section III). Figure 6d shows that for a fixed idler ($\mu = 7$ at 1528 nm), the pump-off-resonance noise has a linear dependence on the pump power while the resonant noise is clearly nonlinear. Since the conversion efficiency is determined by the product of two pump powers, and the 980 nm pump is expected to generate little noise in the 1550 nm band due to the large spectral separation, it seems possible to improve the SNR dramatically by using a relatively large 980 nm pump (e.g., 40 mW) and a smaller 1550 nm pump (e.g., 10 mW). Optimizing the noise performance of this downconversion interface will be a subject of future studies.

Discussion We have demonstrated efficient single-photon-level frequency conversion through four-wave-mixing Bragg scattering (FWM-BS) in monolithic Si_3N_4 microring resonators. In contrast to parametric amplification (PA), which is the basis of the majority of prior work in Kerr-based nanophotonic devices[7], FWM-BS avoids spontaneous emission noise and can be, in principle, noiseless[18]. We have demonstrated background noise powers in the fW to pW range, and potential routes to reduce this further have been identified. The performance of these devices is already comparable to what has been demonstrated for FWM-BS in highly nonlinear fibers and photonic crystal fibers and in some respects, such as pump power required and extent of the spectral translation range, exceeds them. Moreover, the versatility of the FWM-BS process has been demonstrated. Because the frequency translation range is set by the difference in pump frequencies (in contrast to frequency conversion by either PA or the $\chi^{(2)}$ nonlinearity), our devices enable both intraband conversion (translation range between 1.8 nm and 9.0 nm shown with no degradation in performance) and interband conversion (upconversion and downconversion over a translation range $>$560 nm). These devices are already suitable for proof-of-principle QFC experiments with single photon Fock states, and the concepts we utilize - dispersion engineering to ensure frequency matching and tailored waveguide coupling to ensure efficient injection of the signal and pumps and extraction of the converted idler - can be readily applied to connect visible-wavelength quantum light sources (e.g., based on color centers in diamond or trapped atoms and ions) with the telecommunications band.

There are several topics to be addressed in the pursuit of such goals. The use of a resonantly-enhanced process comes at the expense of bandwidth, which is set by the cavity linewidth $\kappa/2\pi \approx 1.3$ GHz in both the 980 nm and 1550 nm bands. Importantly, this bandwidth is large enough to accommodate the photons generated by single InAs/GaAs quantum dots[35], our intended target application, and recently demonstrated quantum light sources in the Si_3N_4 platform would also be compatible[37,38]. The GHz bandwidth stands in contrast to compact wavelength converters based on cavity optomechanics[39–41], which have been limited to the MHz range (at most). Nevertheless, even with a sufficiently large bandwidth, the precise temporal profile of the incoming photon's wavepacket is an important consideration when determining the efficiency with which it can be coupled into the frequency conversion cavity[42,43]. More generally, bandwidth and temporal shaping to efficiently load the cavity are topics that will need to be considered when moving from frequency conversion of continuous-wave signals to pulsed light. Finally, while

the focus of our discussion has been on the demanding application of QFC, the potential classical applications of this work are also significant. This includes add-drop wavelength multiplexing and cross-connect switching that utilize the interband FWM-BS process, and spectral translation of signals across hundreds of nanometers to connect, for example, atomic frequency references with telecommunications-band signals.

Methods

Device fabrication First, the layer stack is created by low-pressure chemical vapor deposition of a 480 nm thick Si_3N_4 layer on top of a 3 μm thick SiO_2 layer, which in turn was grown via thermal oxidation of a 100 mm Si wafer. The wavelength-dependent refractive index and thickness of the layers are determined using a spectroscopic ellipsometer, with the data fit to an extended Sellmeier model. After dicing into chips, the microring-waveguide devices are created by electron-beam lithography of a negative tone resist, followed by reactive ion etching of the Si_3N_4 using a CF_4/CHF_3 chemistry, removal of deposited polymer and remnant resist, and annealing at 1150 °C in an O_2 environment for 3 hours.

Numerical simulation The simulations presented in this work are based on coupled mode equations as well as a modified LLE method. For the 980 nm intraband conversion, we first study a simplified set of coupled mode equations (which neglects pump mixing in the 1550 nm band and high-order idler generation in the 980 nm band) to gain some physical insight (Supplementary Section I.A.), from which the mode splitting observed in the experiment (Fig. 3b, case IV) can be easily understood. Next, a modified LLE method is developed (Supplementary Section I.C), which is essentially a systematic way to implement the same coupled mode equations by including a complete set of resonant modes. The simulation results shown in Figs. 4a and 4c show good agreement between the LLE simulation and the experimental results, indicating it has captured all relevant physical mechanisms. As for the wideband frequency conversion between the 1550 nm and 980 nm bands, since the pump mixing is absent, the LLE method is expected to generate almost the same results as the coupled mode equations. We use the coupled mode equations to study the device's performance, as its numerical computation is much faster than the LLE method (Supplementary I.B). Additional discussions on the upconversion and the effect of pump detunings to the frequency conversion process are also provided in the Supplementary Material (Section IV).

Frequency conversion metrics We characterize our frequency conversion devices based on their on-chip conversion efficiency, noise power, signal-to-noise ratio for a single-photon-level input, and required pump power. The on-chip conversion efficiency is defined as the ratio of a given idler's photon flux at the coupling waveguide output to the signal photon flux at the coupling waveguide input. The background noise power is defined as the power at a given idler's spectral position taken over a specified bandwidth (determined by a narrowband filter) and with the input signal switched off and both pumps turned on. The SNR for single-photon-level inputs is estimated by attenuating the input signal level to a photon flux consistent with that achieved by quantum dot single photon sources (e.g., 1 pW $\approx 5\times10^6$ s^{-1}), and measuring the photon flux in a given idler band with both the signal on and off. Finally, the pump powers listed are on-chip and at the waveguide input.

* Electronic address: qing.li@nist.gov
† Electronic address: kartik.srinivasan@nist.gov

[1] R. W. Boyd, *Nonlinear optics* (Academic press, 2003).
[2] G. P. Agrawal, *Nonlinear Fiber Optics* (Academic Press, Amsterdam, 2007).
[3] C. Langrock, E. Diamanti, R. Roussev, Y. Yamamoto, M. Fejer, and H. Takesue, "Highly efficient single-photon detection at communication wavelengths by use of upconversion in reverse-proton-exchanged periodically poled $LiNbO_3$ waveguides," Optics Letters **30**, 1725–1727 (2005).
[4] A. H. Gnauck, R. Jopson, C. McKinstrie, J. Centanni, and S. Radic, "Demonstration of low-noise frequency conversion by Bragg scattering in a fiber," Optics Express **14**, 8989–8994 (2006).
[5] P. Kumar, "Quantum Frequency-Conversion," Optics Letters **15**, 1476–1478 (1990).
[6] M. G. Raymer and K. Srinivasan, "Manipulating the color and shape of single photons," Physics Today **65**, 32–37 (2012).
[7] D. J. Moss, R. Morandotti, A. L. Gaeta, and M. Lipson, "New CMOS-compatible platforms based on silicon nitride and Hydex for nonlinear optics," Nature Photonics **7**, 597–607 (2013).
[8] M. A. Foster, A. C. Turner, J. E. Sharping, B. S. Schmidt, M. Lipson, and A. L. Gaeta, "Broad-band optical parametric gain on a silicon photonic chip," Nature **441**, 960–963 (2006).
[9] P. DelHaye, A. Schliesser, O. Arcizet, T. Wilken, R. Holzwarth, and T. Kippenberg, "Optical frequency comb generation from a monolithic microresonator," Nature **450**, 1214–1217 (2007).
[10] A. C. Turner, M. A. Foster, A. L. Gaeta, and M. Lipson, "Ultra-low power parametric frequency conversion in a silicon microring resonator," Optics Express **16**, 4881–4887 (2008).
[11] J. S. Levy, A. Gondarenko, M. A. Foster, A. C. Turner-Foster, A. L. Gaeta, and M. Lipson, "CMOS-compatible multiple-wavelength oscillator for on-chip optical interconnects," Nature Photonics **4**, 37–40 (2010).
[12] L. Razzari, D. Duchesne, M. Ferrera, R. Morandotti, S. Chu, B. Little, and D. Moss, "CMOS-compatible integrated optical hyper-parametric oscillator," Nature Photonics **4**, 41–45 (2010).
[13] X. Liu, R. M. Osgood, Y. A. Vlasov, and W. M. Green, "Mid-infrared optical parametric amplifier using silicon nanophotonic waveguides," Nature Photonics **4**, 557–560 (2010).
[14] S. Zlatanovic, J. S. Park, S. Moro, J. M. C. Boggio, I. B. Divliansky, N. Alic, S. Mookherjea, and S. Radic, "Mid-infrared wavelength conversion in silicon waveguides using ultracompact telecom-band-derived pump source," Nature Photonics **4**, 561–564 (2010).
[15] C. McKinstrie, M. Yu, M. Raymer, and S. Radic, "Quantum noise properties of parametric processes," Optics Express **13**, 4986–5012 (2005).
[16] M. E. Marhic, F. Yang, L. Kazovsky, and Y. Park, "Widely tunable spectrum translation and wavelength exchange by four-wave mixing in optical fibers," Optic Letters **21**, 1906–1908 (1996).
[17] K. Uesaka, K. Kin-Yip, M.E., Marhic, and L. Kazovsky, "Wavelength exchange in a highly nonlinear dispersion-shifted fiber: Theory and experiments," IEEE J. Sel. Top. Quan. Elec. **8**, 560–568 (2002).
[18] C. McKinstrie, J. Harvey, S. Radic, and M. Raymer, "Translation of quantum states by four-wave mixing in fibers," Opt. Express **13**, 9131–9142 (2005).
[19] S. Lefrancois, A. S. Clark, and B. J. Eggleton, "Optimizing optical Bragg scattering for single-photon frequency conversion,"

Physical Review A **91**, 013 837 (2015).

[20] I. Agha, M. Davanço, B. Thurston, and K. Srinivasan, "Low-noise chip-based frequency conversion by four-wave-mixing Bragg scattering in SiNx waveguides," Optics Letters **37**, 2997–2999 (2012).

[21] I. Agha, S. Ates, M. Davanço, and K. Srinivasan, "A chip-scale, telecommunications-band frequency conversion interface for quantum emitters," Optics Express **21**, 21 628–21 638 (2013).

[22] Y. Huang, V. Velev, and P. Kumar, "Quantum frequency conversion in nonlinear microcavities," Optics Letters **38**, 2119–2121 (2013).

[23] Z. Lin, S. G. Johnson, A. W. Rodriguez, and M. Loncar, "Design of diamond microcavities for single photon frequency down-conversion," Optics Express **23**, 25 279–25 294 (2015).

[24] H. J. McGuinness, M. G. Raymer, C. J. McKinstrie, and S. Radic, "Quantum Frequency Translation of Single-Photon States in a Photonic Crystal Fiber," Physical Review Letters **105**, 093 604 (2010).

[25] A. S. Clark, S. Shahnia, M. J. Collins, C. Xiong, and B. J. Eggleton, "High-efficiency frequency conversion in the single-photon regime," Optics Letters **38**, 947–949 (2013).

[26] M. Chin and S. Ho, "Design and modeling of waveguide-coupled single-mode microring resonators," Journal of Lightwave Technology **16**, 1433 (1998).

[27] E. Shah Hosseini, S. Yegnanarayanan, A. H. Atabaki, M. Soltani, and A. Adibi, "Systematic design and fabrication of high-Q single-mode pulley-coupled planar silicon nitride microdisk resonators at visible wavelengths," Optics Express **18**, 2127–2136 (2010).

[28] D. T. Spencer, J. F. Bauters, M. J. Heck, and J. E. Bowers, "Integrated waveguide coupled Si3N4 resonators in the ultrahigh-Q regime," Optica **1**, 153–157 (2014).

[29] T. Carmon, L. Yang, and K. Vahala, "Dynamical thermal behavior and thermal self-stability of microcavities," Optics Express **12**, 4742–4750 (2004).

[30] S. Coen, H. G. Randle, T. Sylvestre, and M. Erkintalo, "Modeling of octave-spanning Kerr frequency combs using a generalized mean-field Lugiato–Lefever model," Optics Letters **38**, 37–39 (2013).

[31] A. B. Matsko, A. A. Savchenkov, D. Strekalov, V. S. Ilchenko, and L. Maleki, "Optical hyperparametric oscillations in a whispering-gallery-mode resonator: Threshold and phase diffusion," Physical Review A **71**, 033 804 (2005).

[32] Y. K. Chembo and N. Yu, "Modal expansion approach to optical-frequency-comb generation with monolithic whispering-gallery-mode resonators," Physical Review A **82**, 033 801 (2010).

[33] T. Hansson, D. Modotto, and S. Wabnitz, "On the numerical simulation of Kerr frequency combs using coupled mode equations," Optics Communications **312**, 134–136 (2013).

[34] Y. K. Chembo and C. R. Menyuk, "Spatiotemporal Lugiato-Lefever formalism for Kerr-comb generation in whispering-gallery-mode resonators," Physical Review A **87**, 053 852 (2013).

[35] P. Michler, *Single Semiconductor Quantum Dots* (Springer Verlag, Berlin, 2009).

[36] S. Ates, I. Agha, A. Gulinatti, I. Rech, A. Badolato, and K. Srinivasan, "Improving the performance of bright quantum dot single photon sources using temporal filtering via amplitude modulation," Scientific Reports **3**, 1397 (2013).

[37] A. Dutt, K. Luke, S. Manipatruni, A. L. Gaeta, P. Nussenzveig, and M. Lipson, "On-chip optical squeezing," Physical Review Applied **3**, 044 005 (2015).

[38] S. Ramelow, A. Farsi, S. Clemmen, D. Orquiza, K. Luke, M. Lipson, and A. L. Gaeta, "Silicon-Nitride Platform for Narrowband Entangled Photon Generation," arXiv preprint arXiv:1508.04358 (2015).

[39] C. Dong, V. Fiore, M. C. Kuzyk, and H. Wang, "Optomechanical dark mode," Science **338**, 1609–1613 (2012).

[40] J. T. Hill, A. H. Safavi-Naeini, J. Chan, and O. Painter, "Coherent optical wavelength conversion via cavity optomechanics," Nature Communications **3**, 1196 (2012).

[41] Y. Liu, M. Davanço, V. Aksyuk, and K. Srinivasan, "Electromagnetically Induced Transparency and Wideband Wavelength Conversion in Silicon Nitride Microdisk Optomechanical Resonators," Physical Review Letters **110**, 223 603 (2013).

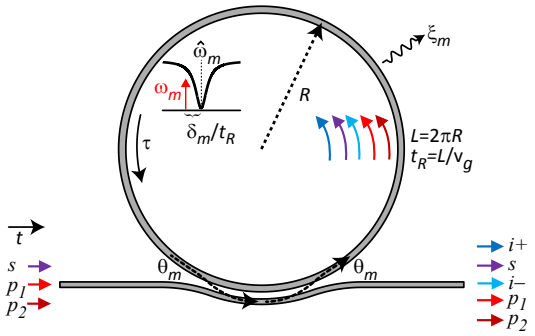
[42] M. Bader, S. Heugel, A. L. Chekhov, M. Sondermann, and G. Leuchs, "Efficient coupling to an optical resonator by exploiting time-reversal symmetry," New Journal of Physics **15**, 123 008 (2013).

[43] C. Liu, Y. Sun, L. Zhao, S. Zhang, M. Loy, and S. Du, "Efficiently loading a single photon into a single-sided Fabry-Perot cavity," Physical Review Letters **113**, 133 601 (2014).

Acknowledgements Q.L. acknowledges support under the Cooperative Research Agreement between the University of Maryland and NIST-CNST, Award 70NANB10H193. The authors thank Lawrence Van Der Vegt from Yenista Optics for the loan of a 1550 nm tunable filter, and Scott Papp from NIST Boulder for helpful comments.

SUPPLEMENTARY MATERIAL

I. THEORY AND NUMERICAL SIMULATIONS



Variable name	Description	Equation
s	input signal	-
$p1$	pump 1	-
$p2$	pump 2	-
$i+$	blue-shifted idler	-
$i-$	red-shifted idler	-
τ	time	-
t	slow time scale set by cavity	-
t_R	cavity round-trip time	-
L	cavity round-trip length	-
ω_m	frequency of driving field near mode m	-
$\hat{\omega}_m$	frequency of mode m	-
E_m	intracavity electric field for mode m	-
E_{in,ω_m}	driving field at frequency ω_m	-
$Q_{i,m}$	intrinsic Q for mode m	-
$Q_{c,m}$	coupling Q for mode m	-
$Q_{L,m}$	total loaded Q for mode m	$Q_{L,m}^{-1}=Q_{i,m}^{-1}+Q_{c,m}^{-1}$
α_m	cavity mode m total loss rate	$\hat{\omega}_m t_R/(2Q_{L,m})$
ξ_m	intrinsic loss rate for mode m	$\hat{\omega}_m t_R/Q_{i,m}$
θ_m	waveguide power coupling rate for mode m	$\hat{\omega}_m t_R/Q_{c,m}$
δ_m	laser-cavity mode m detuning	$\delta_m=(\hat{\omega}_m-\omega_m)t_R$
γ_m	nonlinear coefficient for mode m	see Section I.D

FIG. S1: (Left) Schematic and (Right) table listing the parameters used in the LLE and coupled mode equations models of the four-wave-mixing Bragg scattering process.

The conventional LLE formalism describes the Kerr nonlinearity in a $\chi^{(3)}$ microring resonator as [1,2]

$$t_R\frac{\partial E(t,\tau)}{\partial t}=\left[-\alpha-i\delta_0+iL\sum_{k\geq 2}\frac{\beta_k}{k!}\left(i\frac{\partial}{\partial\tau}\right)^k+i\gamma L|E(t,\tau)|^2\right]E(t,\tau)+i\sqrt{\theta}E_{\rm in}, \tag{S1}$$

where t_R is the round-trip time, $E(t,\tau)$ is the intracavity mean field with $|E(t,\tau)|^2$ representing the average power traveling inside the cavity (τ is the time and t is a parameter measuring the slow time of the cavity), α and δ_0 are the total cavity loss and detuning at the resonance frequency $\hat{\omega}_0$, respectively ($\alpha=\hat{\omega}_0 t_R/(2Q_L)$ with Q_L being the loaded Q and $\delta_0=(\hat{\omega}_0-\omega_0)t_R$ with ω_0 being the frequency of the driving field), L is the round-trip length of the resonator, $\beta_k (k\geq 2)$ are the second and higher-order dispersion parameters of the ring waveguide, γ is the Kerr nonlinear coefficient, θ is the power coupling coefficient between the resonator and the access waveguide or fiber ($\theta=\hat{\omega}_0 t_R/Q_c$ with Q_c being the coupling Q), and $E_{\rm in}$ is a continuous-wave driving field (input power $P_{\rm in}=|E_{\rm in}|^2$). Figure S1 schematically depicts the system under investigation, and includes a table of the aforementioned variables.

As mentioned in the main paper, the LLE formalism is equivalent to coupled mode equations [3,4]. In fact, $E(t,\tau)$ can be viewed as a collection of resonant modes $\{E_m(t)\}$ (m is the azimuthal order) oscillating on an equally spaced frequency grid $\{\omega_m\}$ ($E(t,\tau)=\sum_m E_m(t)\exp(-i\omega_m\tau)$), whose governing coupled mode equation can be obtained through a Fourier transform of Eq. S1. However, for the FWM-BS process we have three driving fields (instead of only one pump in the standard LLE formalism), and each can have its own detuning with respect to the nearest cavity mode. Thus, the coupled mode equations should present the following form:

$$t_R\frac{dE_m}{dt}=-(\alpha_m+i\delta_m)E_m+i\gamma_m L\mathcal{F}\left\{|E(t,\tau)|^2E(t,\tau)\right\}_m+i\sqrt{\theta_m}E_{{\rm in},m}, \tag{S2}$$

where $\mathcal{F}$ stands for the Fourier transform, and all the parameters and expressions with subscript m are meant to be computed at frequency ω_m. In particular, the detuning parameter δ_m is given by $\delta_m=(\hat{\omega}_m-\omega_m)t_R$, where the resonance frequency $\hat{\omega}_m$ is determined by a self-consistent equation $\hat{\omega}_m=\hat{\omega}_0+\sum_{k\geq 1}L\beta_k(\hat{\omega}_m-\hat{\omega}_0)^k/(k!t_R)$. In the experiment, the frequencies of the driving fields for the two pumps and the signal ($\omega_{p1,p2,s}$) are free parameters that can be varied to achieve an optimum frequency conversion efficiency. On the other hand, the frequency of the generated idlers ($\omega_{i\pm}$) is determined by the energy conservation condition, and therefore is a function of $\omega_{p1,p2,s}$ (see Fig. 1c for the 980 nm intraband conversion and Fig. 5 for wideband conversion in the main paper).

In the following, we will discuss the detailed implementations of coupled mode equations as well as a modified LLE method for the FWM-BS process.

A. Coupled mode equations for 980 nm intraband conversion

We start with a simplified set of coupled mode equations for the intraband frequency conversion in the 980 nm band, that is, we neglect pump mixing in the 1550 nm band and high-order idlers in the 980 nm band. As a result, the modes under consideration are: two pumps ($p1$ and $p2$), the signal (s), and two idlers ($i+$ and $i-$). Following Eq. S2, the coupled mode equation for pump 1 can be written as

$$t_R \frac{dE_{p1}}{dt} = -(\alpha_{p1} + i\Delta\phi_{p1})E_{p1} + i\sqrt{\theta_{p1}P_{p1}}, \tag{S3}$$

where we have combined δ_{p1} and the Kerr nonlinear shift into an effective detuning $\Delta\phi_{p1}$, which is given by

$$\Delta\phi_{p1} = (\hat{\omega}_{p1} - \omega_{p1})t_R - \gamma_{p1}L(|E_{p1}|^2 + 2|E_{p2}|^2). \tag{S4}$$

For a steady state, Eq. S3 gives $E_{p1} = i\sqrt{\theta_{p1}P_{p1}}/(\alpha_{p1} + i\Delta\phi_{p1})$. Similarly, for pump 2 we obtain $E_{p2} = i\sqrt{\theta_{p2}P_{p2}}/(\alpha_{p2} + i\Delta\phi_{p2})$ and its effective detuning $\Delta\phi_{p2}$ as

$$\Delta\phi_{p2} = (\hat{\omega}_{p2} - \omega_{p2})t_R - \gamma_{p2}L(2|E_{p1}|^2 + |E_{p2}|^2). \tag{S5}$$

Next, we derive the coupled mode equations for the signal and idlers as

$$t_R \frac{dE_s}{dt} = -(\alpha_s + i\Delta\phi_s)E_s + i2\gamma_s L E_{p1}E_{p2}^* E_{i-} + i2\gamma_s L E_{p1}^* E_{p2} E_{i+} + i\sqrt{\theta_s P_s}, \tag{S6}$$

$$t_R \frac{dE_{i+}}{dt} = -(\alpha_{i+} + i\Delta\phi_{i+})E_{i+} + i2\gamma_{i+} L E_{p1}E_{p2}^* E_s, \tag{S7}$$

$$t_R \frac{dE_{i-}}{dt} = -(\alpha_{i-} + i\Delta\phi_{i-})E_{i-} + i2\gamma_{i-} L E_{p1}^* E_{p2} E_s, \tag{S8}$$

with their effective detunings given by

$$\Delta\phi_s = (\hat{\omega}_s - \omega_s)t_R - 2\gamma_s L(|E_{p1}|^2 + |E_{p2}|^2), \tag{S9}$$

$$\Delta\phi_{i+} = (\hat{\omega}_{i+} - \omega_{i+})t_R - 2\gamma_{i+} L(|E_{p1}|^2 + |E_{p2}|^2), \tag{S10}$$

$$\Delta\phi_{i-} = (\hat{\omega}_{i-} - \omega_{i-})t_R - 2\gamma_{i-} L(|E_{p1}|^2 + |E_{p2}|^2). \tag{S11}$$

Because of energy conservation, $\omega_{i\pm} = \omega_s \pm |\omega_{p1} - \omega_{p2}|$. Using Eqs. S4, S5, and S9, we can express the detunings of the two idlers as

$$\Delta\phi_{i+} = (\hat{\omega}_{i+} - \hat{\omega}_s - \left|\hat{\omega}_{p1} - \hat{\omega}_{p2}\right|)t_R + \Delta\phi_s + (\Delta\phi_{p1} - \Delta\phi_{p2}) - \gamma^{1550} L(|E_{p1}|^2 - |E_{p2}|^2), \tag{S12}$$

$$\Delta\phi_{i-} = (\hat{\omega}_{i-} - \hat{\omega}_s + \left|\hat{\omega}_{p1} - \hat{\omega}_{p2}\right|)t_R + \Delta\phi_s - (\Delta\phi_{p1} - \Delta\phi_{p2}) + \gamma^{1550} L(|E_{p1}|^2 - |E_{p2}|^2), \tag{S13}$$

where we have used the approximation $\gamma_s \approx \gamma_{i+} \approx \gamma_{i-} \approx \gamma^{980}$, since the signal and idlers are close in wavelength. Likewise, for the two pumps, $\gamma_{p1} \approx \gamma_{p2} \approx \gamma^{1550}$. It it worth noting that the frequency detuning $\delta\hat{\omega}_\pm$ defined in the main paper is proportional to the first part of $\Delta\phi_{i\pm}$, as in our experiment (Fig. 3 in the main paper) the two pumps are operated under similar conditions ($P_{p1} \approx P_{p2}$ and $\Delta\phi_{p1} \approx \Delta\phi_{p2}$) and the signal is typically set at the minimum of its transmission ($\Delta\phi_s \approx 0$), thus making the first part the dominant term.

TABLE I: Additional variables used in the coupled mode equations

Variable name	Description	Equation
$\Delta\phi_{p1}$	Effective detuning for pump 1	Eq. 4
$\Delta\phi_{p2}$	Effective detuning for pump 2	Eq. 5
$\Delta\phi_s$	Effective detuning for the input signal	Eq. 9
$\Delta\phi_{i+}$	Effective detuning for the blue-shifted idler	Eqs. 10 and 12
$\Delta\phi_{i-}$	Effective detuning for the red-shifted idler	Eqs. 11 and 13
Ω_0	Effective nonlinear parameter	$\Omega_0 = 2\gamma^{980}L\lvert E_{p1}E_{p2}\rvert$
Ω_1	Asymmetry in idler detuning	$(\Delta\phi_{i+} - \Delta\phi_{i-})/2$
Ω_2	Mean idler detuning	$(\Delta\phi_{i+} + \Delta\phi_{i-})/2$

The coupled mode equations (Eqs. S6-S8) generally have three eigenmodes with different eigenfrequencies, readily suggesting mode splitting in the transmission. To gain some insight, we carry out a brief analytical study here. First, we define three parameters: $\Omega_0 \equiv 2\gamma^{980}L|E_{p1}E_{p2}|$, $\Omega_1 \equiv (\Delta\phi_{i+} - \Delta\phi_{i-})/2$, and $\Omega_2 \equiv (\Delta\phi_{i+} + \Delta\phi_{i-})/2$. Using the result of $\delta\hat{\omega}_\pm$ obtained in the main paper (i.e., $\delta\hat{\omega}_{\pm|\mu|} \approx \pm\delta D_1|\mu| + \frac{1}{2}\delta D_{2,\mp}\mu^2$, where μ stands for the azimuthal order difference between the two pumps), we arrive at

$$\Omega_1 \approx \delta D_1|\mu|t_R - \frac{1}{2}D_2^{1550}\mu^2 t_R + \Delta\phi_{p1} - \Delta\phi_{p2} - \gamma^{1550}L(|E_{p1}|^2 - |E_{p2}|^2), \tag{S14}$$

$$\Omega_2 \approx \frac{1}{2}D_2^{980}\mu^2 t_R. \tag{S15}$$

One can easily identify the factors affecting Ω_1 are: the FSR mismatch between the 1550 nm and 980 nm bands, the second order dispersion in the 1550 nm band, and the experimental operating conditions of the two 1550 nm pumps (especially the symmetry). Ω_2, on the other hand, is generally small and purely determined by the dispersion of the 980 nm band (in particular, it is independent of the two pump settings). Here we approximate $\Omega_2 \approx 0$, and the three eigenfrequencies can be calculated as

$$\hat{\omega}_{e1} \approx \hat{\omega}_s, \tag{S16}$$

$$\hat{\omega}_{e2} \approx \hat{\omega}_s + \frac{1}{t_R}\sqrt{2\Omega_0^2 + \Omega_1^2}, \tag{S17}$$

$$\hat{\omega}_{e3} \approx \hat{\omega}_s - \frac{1}{t_R}\sqrt{2\Omega_0^2 + \Omega_1^2}. \tag{S18}$$

It is also interesting to find the corresponding eigenmodes, which are

$$|\mathbf{e}_1\rangle = N_1\left(\frac{1}{\sqrt{1+2\eta^2}}|\mathbf{s}\rangle - \frac{\eta}{\sqrt{1+2\eta^2}}|\mathbf{i}+\rangle + \frac{\eta}{\sqrt{1+2\eta^2}}|\mathbf{i}-\rangle\right), \tag{S19}$$

$$|\mathbf{e}_2\rangle = N_2\left(|\mathbf{s}\rangle + \frac{\eta}{\sqrt{1+2\eta^2}-1}|\mathbf{i}+\rangle + \frac{\eta}{\sqrt{1+2\eta^2}+1}|\mathbf{i}-\rangle\right), \tag{S20}$$

$$|\mathbf{e}_3\rangle = N_3\left(|\mathbf{s}\rangle - \frac{\eta}{\sqrt{1+2\eta^2}+1}|\mathbf{i}+\rangle - \frac{\eta}{\sqrt{1+2\eta^2}-1}|\mathbf{i}-\rangle\right), \tag{S21}$$

where $\eta \equiv \Omega_0/\Omega_1$ and N_k is a normalization factor for $|\mathbf{e}_k\rangle$ to ensure $\langle \mathbf{e}_k|\mathbf{e}_k\rangle = 1$ ($k = 1,2,3$). Generally, the state of photons travelling inside the cavity will be a superposition of the these three eigenmodes, with the coefficients determined by parameters including α_s (cavity linewidth) and [Ω_0 Ω_1 Ω_2]. Down to single photon level, the square of the coefficient associated with each eigenmode can be interpreted as the probability of finding the injected photon in this particular mode.

Next, numerical simulations are carried out in Fig. S2 to investigate the effect of different combinations of [Ω_0 Ω_1 Ω_2] to the frequency conversion process (the two pumps are assumed to have equal power and detuning). Figure S2a plots the reference example, which corresponds to the device under study for a pump power of 30 mW per pump. The transmission scan of the signal resonance (left figure) and the conversion efficiency for the blue and red idlers (right figure) as a function of signal detuning are similar to the experimental results (Fig. 3b, case IV) and the LLE simulation (Fig. 4c) shown in the main paper. The asymmetric mode splitting observed in the transmission scan is due to a nonzero Ω_2, which is negative for our device (see Eq. S15 and note $D_2^{980} < 0$ since the resonator shows normal dispersion in both 1550 nm and 980 nm bands). If Ω_2 is positive, as illustrated by Fig. S2b, the asymmetry in the transmission scan is mirrored in the spectrum, whereas a symmetric mode splitting is expected if Ω_2 is zero.

Figures S2c-d explore how the pump power affects the frequency conversion process (varying Ω_0), which shows that the maximum conversion efficiency for both blue and red idlers is limited to ≈ -5 dB for pump powers larger than 16 mW. In addition, as the pump power increases, the mode splitting becomes stronger and the optimum signal detuning corresponding to the maximum conversion efficiency for the blue and red idlers shifts away from origin. Therefore, if we choose to use a fixed signal detuning (such as zero), the conversion efficiency will start to decrease with the pump power after reaching its optimum value[5]. Finally, Figs. S2e-f study the effect of Ω_1, that is, the asymmetry in the idler detunings with respect to the nearest cavity modes. According to Eq. S14, its absolute value can be easily comparable to the cavity loss rate if the separation between the two 1550 nm pumps ($|\mu|$) or the FSR mismatch between the 1550 nm and 980 nm bands is large enough. In addition, its value can change significantly if the two pumps are operated under different conditions (such as $P_{p2} \gg P_{p1}$ as in the wideband conversion experiment shown in the main paper). The simulation shows that as $|\Omega_1|$ increases (Fig. S2e), we start to see three dips in the transmission scan, corresponding to the three eigenmodes of the coupled system (a similar spectrum has been observed in the experiment for a different device, though the data not is shown here). Moreover, unlike the previous examples (Figs. S2a-d) where the blue and red idlers show similar conversion efficiencies, in this case only one idler can reach its maximum conversion efficiency while the other one is much weaker. Further increasing $|\Omega_1|$ (Fig. S2f) results in a bigger contrast between the blue and red idlers if one of them is set at its optimum conversion efficiency. However, if $|\Omega_1|$ is too large ($> 5\alpha_s$ for the pump power of 30 mW), the maximum achievable conversion efficiency for both idlers drops significantly (< 10 %), and the transmission scan of the signal resonance starts to look like the linear case.

B. Coupled mode equations for wideband frequency conversion

The coupled mode equations for the wideband frequency conversion can be derived following a similar fashion as in the previous subsection. Especially, as demonstrated by Fig. 5d in the main paper, the pump mixing is absent in the wideband conversion case since the two pumps are widely separated. Consequently, other than the two pumps, there are typically four modes: the signal (s), the auxiliary tone generated from the mixing of the signal and its nearby pump (s'), and two idlers ($i+$ and $i-$). The coupled mode equations developed here will only consider these four modes, which means we neglect higher order idlers generated from the mixing of $i\pm$ with its nearby pump.

To treat both the upconversion and downconversion, we label the two modes in the 980 nm band as a and b, and the two modes in the 1550 nm band as c and d (see Fig. S3). For the upconversion case, [a b c d] correspond to [$i+$ $i-$ s s'], respectively. For the downconversion case, [a b c d] correspond to [s s' $i+$ $i-$], respectively.

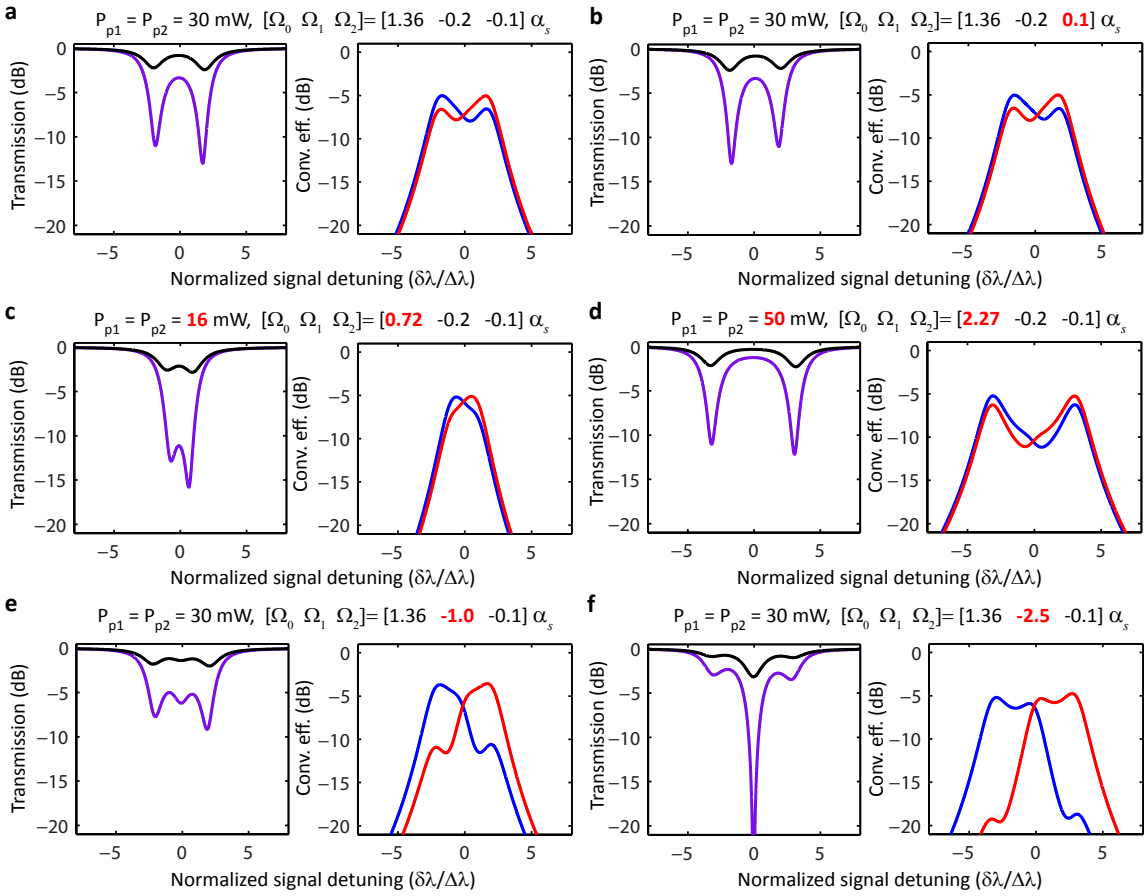


FIG. S2: **Coupled mode simulations for the 980 nm intraband conversion**. **a** Reference example of the parameter variations of $[\Omega_0\ \Omega_1\ \Omega_2]$ in units of α_s (cavity loss rate at the signal resonance). The varied parameter in other cases is highlighted. For each case, the left figure shows the transmission (purple: signal only; black: signal plus two idlers) and the right figure shows the on-chip conversion efficiency (blue for $i+$ and red for $i-$) as a function of normalized signal detunings ($-\Delta\phi_s/\alpha_s = \delta\lambda/\Delta\lambda$ where $2\Delta\lambda \approx 4$ pm is the linewidth of the signal resonance). **b**, Changing the sign of Ω_2 will reverse the symmetry between the two split modes in the transmission scan. **c-d**,Varying Ω_0 (i.e., the pump power): mode splitting increases with the pump power. **e-f**, Varying Ω_1: nonzero $|\Omega_1|$ removes the degeneracy in the conversion efficiency between $i+$ and $i-$; especially, a relatively large $|\Omega_1|$ can make one idler much stronger than the other at its optimum signal detuning.

First, we consider the case without the signal input field driving its cavity resonance. The coupled mode equations for these four modes can be written as

$$t_R\frac{dE_a}{dt} = -(\alpha_{p1}+i\Delta\phi_a)E_a + i\gamma_{p1}LE_{p1}^2E_b^* + i2\gamma_{p1}LE_{p1}(E_{p2}E_d^* + E_{p2}^*E_c), \tag{S22}$$

$$t_R\frac{dE_b}{dt} = -(\alpha_{p1}+i\Delta\phi_b)E_b + i\gamma_{p1}LE_{p1}^2E_a^* + i2\gamma_{p1}LE_{p1}(E_{p2}E_c^* + E_{p2}^*E_d), \tag{S23}$$

$$t_R\frac{dE_c}{dt} = -(\alpha_{p2}+i\Delta\phi_c)E_c + i\gamma_{p2}LE_{p2}^2E_d^* + i2\gamma_{p2}LE_{p2}(E_{p1}E_b^* + E_{p1}^*E_a), \tag{S24}$$

$$t_R\frac{dE_d}{dt} = -(\alpha_{p2}+i\Delta\phi_d)E_d + i\gamma_{p2}LE_{p2}^2E_c^* + i2\gamma_{p2}LE_{p2}(E_{p1}E_a^* + E_{p1}^*E_b), \tag{S25}$$

where for simplicity we have approximated α and γ of each wave as the values of its nearby pump (e.g., $\gamma_{a,b} = \gamma_{p1}$ and $\gamma_{c,d} = \gamma_{p2}$). In addition, the effective detunings of these modes are obtained as

$$\Delta\phi_a = (\hat{\omega}_a - \omega_a)t_R - 2\gamma_{p1}L(|E_{p1}|^2 + |E_{p2}|^2), \tag{S26}$$

$$\Delta\phi_b = (\hat{\omega}_b - \omega_b)t_R - 2\gamma_{p1}L(|E_{p1}|^2 + |E_{p2}|^2), \tag{S27}$$

$$\Delta\phi_c = (\hat{\omega}_c - \omega_c)t_R - 2\gamma_{p2}L(|E_{p1}|^2 + |E_{p2}|^2), \tag{S28}$$

$$\Delta\phi_d = (\hat{\omega}_d - \omega_d)t_R - 2\gamma_{p2}L(|E_{p1}|^2 + |E_{p2}|^2). \tag{S29}$$

Similar to the 980 nm intraband conversion, the energy conservation condition (see Fig. 5 in the main paper) is used to express the detunings of the idlers as a function of the signal and pump detunings, which are free parameters to be varied in the experiment. For example, for the

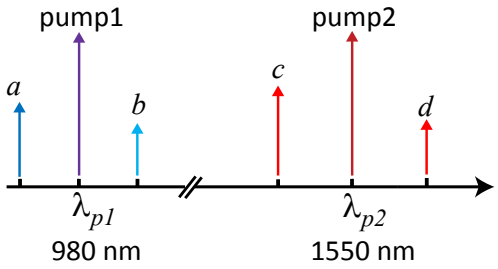


FIG. S3: **Schematic of the wideband conversion process.** This schematic shows the four modes under consideration in the coupled mode equations for the wideband frequency conversion. For the upconversion, c is the signal, d is the auxiliary tone resulting from the wave mixing between c and pump 2, and a and b are $i+$ and $i-$, respectively. For the downconversion, a is the signal, b is the auxiliary tone resulting from the wave mixing between a and pump 1, and c and d are $i+$ and $i-$, respectively.

upconversion case, energy conservation requires $\omega_a = \omega_{p1} + |\omega_c - \omega_{p2}|$, $\omega_b = \omega_{p1} - |\omega_c - \omega_{p2}|$, and $\omega_d = 2\omega_{p2} - \omega_c$. With some algebra, we arrive at

$$\Delta\phi_a = [(\hat{\omega}_a - \hat{\omega}_{p1}) - (\hat{\omega}_c - \hat{\omega}_{p2})]t_R + \Delta\phi_c + (\Delta\phi_{p1} - \Delta\phi_{p2}) - (\gamma_{p1}L|E_{p1}|^2 - \gamma_{p2}L|E_{p2}|^2), \tag{S30}$$

$$\Delta\phi_b = [(\hat{\omega}_b - \hat{\omega}_{p1}) + (\hat{\omega}_c - \hat{\omega}_{p2})]t_R - \Delta\phi_c + (\Delta\phi_{p1} + \Delta\phi_{p2}) - (\gamma_{p1}L|E_{p1}|^2 + \gamma_{p2}L|E_{p2}|^2), \tag{S31}$$

$$\Delta\phi_d = [\hat{\omega}_d + \hat{\omega}_c - 2\hat{\omega}_{p2}]t_R - \Delta\phi_c + 2\Delta\phi_{p2} - 2\gamma_{p2}L|E_{p2}|^2. \tag{S32}$$

In the same way, for the downconversion case (a is the signal), we have $\omega_c = \omega_{p2} + |\omega_a - \omega_{p1}|$, $\omega_d = \omega_{p2} - |\omega_a - \omega_{p1}|$, and $\omega_b = 2\omega_{p1} - \omega_a$. The effective detunings of these modes can then be derived as

$$\Delta\phi_c = [(\hat{\omega}_c - \hat{\omega}_{p2}) - (\hat{\omega}_a - \hat{\omega}_{p1})]t_R + \Delta\phi_a - (\Delta\phi_{p1} - \Delta\phi_{p2}) + (\gamma_{p1}L|E_{p1}|^2 - \gamma_{p2}L|E_{p2}|^2), \tag{S33}$$

$$\Delta\phi_d = [(\hat{\omega}_d - \hat{\omega}_{p2}) + (\hat{\omega}_a - \hat{\omega}_{p1})]t_R - \Delta\phi_a + (\Delta\phi_{p1} + \Delta\phi_{p2}) - (\gamma_{p1}L|E_{p1}|^2 + \gamma_{p2}L|E_{p2}|^2), \tag{S34}$$

$$\Delta\phi_b = [\hat{\omega}_a + \hat{\omega}_b - 2\hat{\omega}_{p1}]t_R - \Delta\phi_a + 2\Delta\phi_{p1} - 2\gamma_{p1}L|E_{p1}|^2. \tag{S35}$$

Now we add back the driving field for the signal. By defining a vector $\tilde{E}_r = [E_a\ E_b^*\ E_c\ E_d^*]^T$ (the subscript r is to denote that they are fields inside resonator and the superscript T stands for transpose of a matrix), we can write Eqs. S22-S25 into a more compact form as

$$t_R \frac{d\tilde{E}_r}{dt} = \tilde{M}\tilde{E}_r + i\sqrt{\tilde{\Theta}}\tilde{E}_{\text{in}}, \tag{S36}$$

where the matrix $\tilde{M}$ is defined by

$$\tilde{M} \equiv \begin{bmatrix} -\alpha_{p1} - i\Delta\phi_a & i\gamma_{p1}LE_{p1}^2 & i2\gamma_{p1}LE_{p1}E_{p2}^* & i2\gamma_{p1}LE_{p1}E_{p2} \\ -i\gamma_{p1}LE_{p1}^{*2} & -\alpha_{p1} + i\Delta\phi_b & -i2\gamma_{p1}LE_{p1}^*E_{p2}^* & -i2\gamma_{p1}LE_{p1}^*E_{p2} \\ i2\gamma_{p2}LE_{p1}^*E_{p2} & i2\gamma_{p2}LE_{p1}E_{p2} & -\alpha_{p2} - i\Delta\phi_c & i\gamma_{p2}LE_{p2}^2 \\ -i2\gamma_{p2}LE_{p1}^*E_{p2}^* & -i2\gamma_{p2}LE_{p1}E_{p2}^* & -i\gamma_{p2}LE_{p2}^{*2} & -\alpha_{p2} + i\Delta\phi_d \end{bmatrix}, \tag{S37}$$

$\tilde{\Theta}$ is a diagonal matrix defined as $\tilde{\Theta} \equiv \text{diag}(\theta_{p1}\ \theta_{p1}\ \theta_{p2}\ \theta_{p2})$, and $\tilde{E}_{\text{in}}$ is the driving field. For the upconversion case (mode c is the signal), $\tilde{E}_{\text{in}} = [0\ 0\ \sqrt{P_s}\ 0]^T$ and for the downconversion case (mode a is the signal), $\tilde{E}_{\text{in}} = [\sqrt{P_s}\ 0\ 0\ 0]^T$. The steady state solution can be found from Eq. S36 as $\tilde{E}_r = -i\tilde{M}^{-1}\sqrt{\tilde{\Theta}}\tilde{E}_{\text{in}}$ for the fields inside cavity and $\tilde{E}_{\text{WG}} = \tilde{E}_{\text{in}} + i\sqrt{\tilde{\Theta}}\tilde{E}_r$ for the fields at the output of the waveguide. Note that each component of $|\tilde{E}_{\text{WG}}|^2$ represents the power of the corresponding mode, which has to be converted to photon flux for the calculation of the the on-chip conversion efficiency. Simulation examples are provided in Fig. S6c for the upconversion case and Fig. 6b in the main paper for the downconversion case, both showing a good agreement with the experimental results.

C. Modified LLE method for FWM-BS

In this subsection, we will discuss a way to adapt the conventional LLE method for the FWM-BS process. So far, the coupled mode equations presented only consider a few modes. For example, for the intraband conversion in the 980 nm band, we have neglected the pump mixing in the 1550 nm band as well as high-order idler generation in the 980 nm band. It is still possible to include these modes in the coupled mode equations, although the process is typically very manual. By contrast, the LLE formalism can automatically include all resonant modes for the entire wavelength band of interest, making it a convenient tool to study the interaction of multiple modes.

As pointed out at the beginning of this section, in the standard LLE formalism we only set the detuning of the pump (δ_0 in Eq. S1) which is the only driving field[1,2]. In addition, the resonance frequencies of all the modes are referenced to an equally spaced frequency grid $\{\omega_0 + D_1\mu\}$, with D_1 corresponding to the FSR of the pump resonance. In the FWM-BS process, since we have three driving fields (two pumps and one

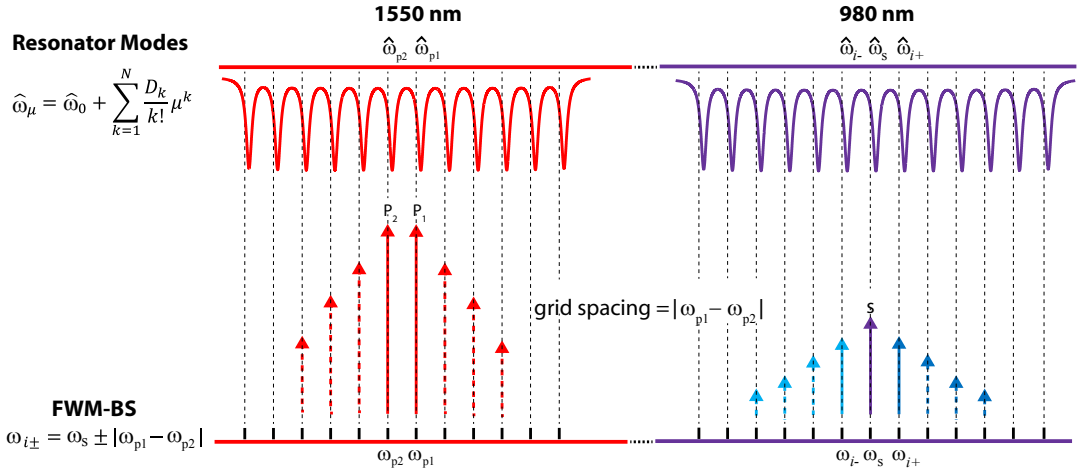


FIG. S4: **Schematic of the frequency grid used in the LLE simulation.** The frequency grid shown here corresponds to the 980 nm intraband conversion with two 1550 nm band pumps accommodated by two adjacent resonances. The vertical dashed arrows in the 1550 nm and 980 nm band represent the secondary pumps generated from the pump mixing and high-order idlers, respectively. The resonator modes are illustrated above, indicating the resonance frequencies are not exactly on the grid due to non-zero detuning and high-order dispersions.

signal), it is not straightforward to allow these three waves have their own detunings independent from the others. In addition, it is also not trivial to choose D_1. For example, even if we decide D_1 should be the FSR of the resonator, we still face the choice of the FSR in the 1550 nm or the 980 nm band.

The solution we find is to implement the LLE formalism based on Eq. S2, whose detuning parameter ($\delta_m = \hat{\omega}_m - \omega_m$) is allowed to vary across different resonant modes. Thus, we can set δ_m corresponding to the two pumps and the signal. The detunings of the remaining modes are determined from the following procedure. First, we obtain resonance frequencies ($\{\hat{\omega}_m\}$) of all the modes from numerical simulations based on an eigenfrequency mode solver for the microresonator under study; second, the equally spaced frequency grid ($\{\omega_m\}$) is set up in the 1550 nm and 980 nm bands separately before joining together. To make it clear, we use the 980 nm intraband conversion as an example (Fig. S4). Assuming the 1550 nm pumps are accommodated by two resonances adjacent to each other (i.e., $m_{p1} - m_{p2} = 1$), the frequency grid in the 980 nm band is chosen as $\omega_m = \omega_s + (m - m_s)|\omega_{p1} - \omega_{p2}|$, where m_s is the azimuthal order of the signal resonance. By doing so, the signal and all the generated idlers automatically fall on the frequency grid (energy conservation satisfied). Similar to the situation in the coupled mode equations, here ω_s, ω_{p1} and ω_{p2} can be replaced by their respective detunings ($\omega_m = \hat{\omega}_m - \delta_m$). Likewise, in the 1550 nm band, we can start with either pump and expand the grid with the same spacing (i.e., $|\omega_{p1} - \omega_{p2}|$). This allows the two 1550 nm pumps and secondary pumps generated from pump mixing to be on the grid, since the energy conservation is automatically satisfied. Finally, we expand the frequency grid in the 980 nm band and the one in the 1550 nm band until they start to overlap the middle of the total frequency span (typically we consider a wavelength range from 900 nm to 1700 nm, so the midpoint is around 1200 nm). Admittedly, there could be some error for the detuning of the joint point (basically ω_m extended from the 980 nm grid is not necessarily equal to that from the 1550 nm grid), but generally this mode is frequency mismatched and far away from the wavelength bands that interest us. As a result, we end up with a frequency grid that spans the whole spectral range, and all the modes of interest are on the grid. Following the same reasoning, if the two 1550 nm pumps are accommodated by resonances with their azimuthal order difference $N = |m_{p1} - m_{p2}| > 1$, we should take the grid spacing as $|\omega_{p1} - \omega_{p2}|/N$. Similarly, for the wideband conversion case, the grid spacing is taken as the frequency difference between the signal and its nearby pump, divided by the difference of their azimuthal orders. Therefore, we can clearly see from this process that the frequency grid spacing is not exactly the FSR of the resonator, with the deviation contributed by nonzero detuning and high-order dispersions.

From the discussion, it should be clear by now that the modified LLE method described above is essentially a systematic way to implement the coupled mode equations discussed in previous subsections (A and B), so that all the resonant modes can be included easily. Other than the detuning, parameters such as α, γ, and θ in Eq. S2 can (and should) be frequency dependent. To solve Eq. S2 numerically, we use the well-known split-step Fourier method, i.e., we calculate the frequency-dependent terms (Eq. S2 without the nonlinear Fourier transformed term) in the frequency domain and then compute the nonlinear term in the time domain. The implementation is similar to that described in Ref. 2.

D. Calculation of Kerr nonlinear coefficient

The purpose of this subsection is to provide a brief discussion on the calculation of the Kerr nonlinear coefficient γ in a nanophotonic structure, as we have noticed there are several different versions existing in the literature [6,7]. We will consider only one wave (the pump) here, as it is fairly straightforward to generalize the result to multiple waves [8,9]. The most common version for γ is probably $\gamma = \frac{n_2\omega}{cA_{\text{eff}}}$ (Ref. 2), where

n_2 is the Kerr nonlinear refractive index ($n_2 \approx 2.5\times10^{-19}$ m^{2}W^{-1} for Si_3N_4), and A_{eff} is the effective mode area given by

$$A_{\text{eff}} = \frac{\left(\int\int |\mathbf{E}(x,y)|^2\, dxdy\right)^2}{\int\int_{\text{core}} |\mathbf{E}(x,y)|^4\, dxdy}, \tag{S38}$$

where $\mathbf{E}(x,y)$ is the electric field of the mode under consideration, and the subscript in the integral denotes the integral over the nonlinear (core) material. This result is typically applied to fibers or waveguides with low index contrast materials.

It is expected that Eq. S38 requires some modification when applied to nanophotonic structures with high index contrast material systems (such as Si_3N_4/SiO_2, Si/SiO_2 or $AlGaAs/SiO_2$). For the $\chi^{(3)}$ process in a microresonator, it has been shown that the effective mode volume is given by [7]

$$V_{\text{eff}} = \frac{\left(\int\int\int \varepsilon_r(\mathbf{r})|\mathbf{E}(\mathbf{r})|^2\, d^3\mathbf{r}\right)^2}{\int\int\int_{\text{core}} \varepsilon_r^2(\mathbf{r})|\mathbf{E}(\mathbf{r})|^4\, d^3\mathbf{r}}, \tag{S39}$$

where ε_r is the relative permittivity. Following this, one may naturally expect that for a waveguide,

$$\bar{A}_{\text{eff}} = \frac{\left(\int\int \varepsilon_r(x,y)|\mathbf{E}(x,y)|^2\, dxdy\right)^2}{\int\int_{\text{core}} \varepsilon_r^2(x,y)|\mathbf{E}(x,y)|^4\, dxdy}. \tag{S40}$$

On the other hand, we can start with the variational principle[10], that is,

$$\delta\beta = \frac{\omega\int\int_{\text{core}} \mathbf{E}^*(x,y)\cdot\mathbf{P}(x,y)\, dxdy}{4P_o}, \tag{S41}$$

where $\mathbf{P}(x,y)$ is the dielectric perturbation and P_o is the power of the waveguide. For the $\chi^{(3)}$ process involving only one wave, we have $\mathbf{P}(x,y) = 3\varepsilon_0\chi^{(3)}_{1111}|\mathbf{E}(x,y)|^2\mathbf{E}(x,y)/4$, where ε_0 is the vacuum permittivity and $\chi^{(3)}_{1111}$ is related to n_2 as $n_2 = 3\chi^{(3)}_{1111}/(4n_0^2\varepsilon_0 c)$ (Ref. **?**), with n_0 being the refractive index of the material. One can easily observe that the nonlinear perturbation results in a power-dependent $\delta\beta$, which is recognized as the self phase modulation. Hence, $\delta\beta = \gamma P_o$. As a result, we end up with $\gamma = \frac{n_2\omega}{c\tilde{A}_{\text{eff}}}$, with a new mode area $\tilde{A}_{\text{eff}}$ defined as

$$\tilde{A}_{\text{eff}} = \frac{4P_o^2}{n_0^2\varepsilon_0^2c^2\int\int_{\text{core}} |\mathbf{E}(x,y)|^4\, dxdy}. \tag{S42}$$

Since the power of the waveguide mode is given by an integral of mode energy density over the waveguide cross section multiplied by the group velocity, we can simplify $\tilde{A}_{\text{eff}}$ as

$$\tilde{A}_{\text{eff}} = \left(\frac{n_0}{n_g}\right)^2 \frac{\left(\int\int \varepsilon_r(x,y)|\mathbf{E}(x,y)|^2\, dxdy\right)^2}{\int\int_{\text{core}} \varepsilon_r^2(x,y)|\mathbf{E}(x,y)|^4\, dxdy}, \tag{S43}$$

which shows there is an additional factor $(n_0/n_g)^2$ compared to $\bar{A}_{\text{eff}}$ in Eq. S40.

We want to point out Eq. S39 is derived based on the same variational principle as Eq. S43. On the other hand, we believe it is not strictly valid to go from Eq. S39 to Eq. S40 for two reasons. First, Eq. S39 is derived for modes with normalized energy, while for waveguides we are dealing with modes normalized by power. The conversion from energy to power introduces a factor proportional to the round-trip time ($t_R = Ln_g/c$) for the $\chi^{(3)}$ nonlinear term. Second, what has been calculated for the waveguide case is $\delta\beta$ caused by the nonlinear perturbation, while the counterpart for the cavity case is the frequency shift $\delta\omega$. They are related by $\delta\beta \approx n_g\delta\omega/c$. Thus, it seems the $(n_0/n_g)^2$ factor can be explained. Nevertheless, for the Si_3N_4 waveguides (that form the ring resonator) studied in this work, the numerical value of $\bar{A}_{\text{eff}}$ is almost the same as $\tilde{A}_{\text{eff}}$, since $n_g \approx n_0 \approx 2$. In comparison, the calculated γ is about 35 % higher than the result based on Eq. S38, suggesting it is important to choose the right mode area for the numerical simulation.

II. PARAMETERS USED IN THE SIMULATION

We list the parameters used in the simulations in the following table.

TABLE II: Parameters used in the simulations

Parameter	1550 nm band	980 nm band	Unit
Q_i	4.5×10^5	9.0×10^5	-
Q_c	2.3×10^5	3.3×10^5	-
Q_L	1.5×10^5	2.4×10^5	-
$D_1/2\pi$	572.39	572.25	GHz
$D_2/2\pi$	-31.04	-3.43	MHz
$D_3/2\pi$	0.71	-0.30	MHz
γ	2.07	3.32	W^{-1}m^{-1}

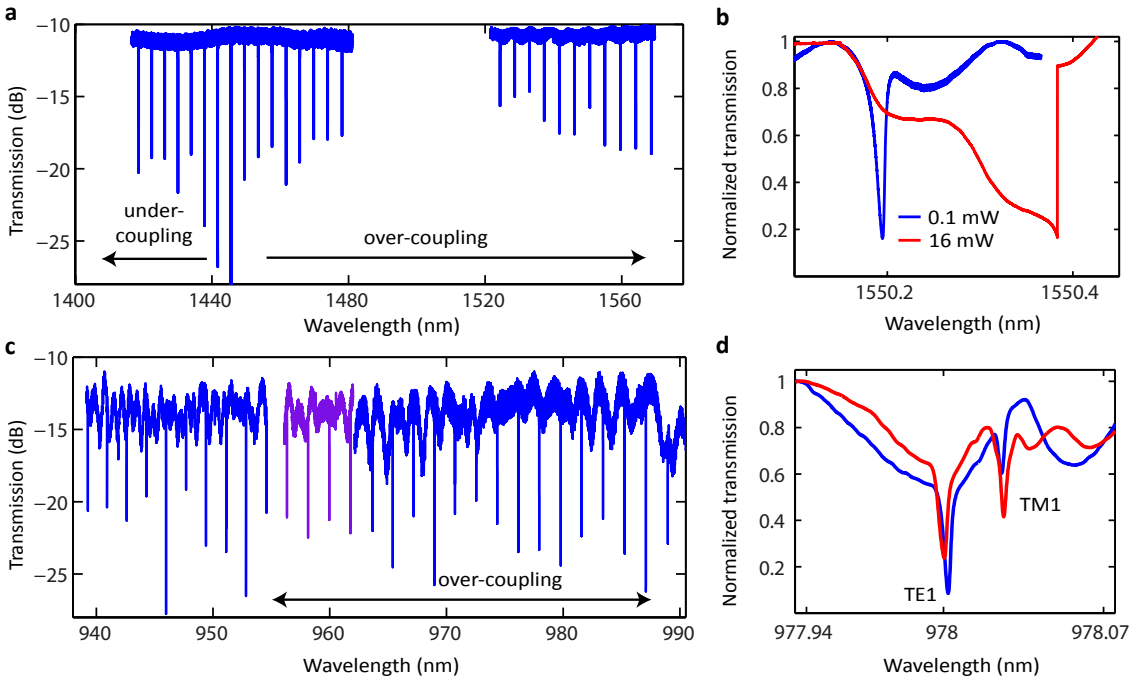


FIG. S5: **Transmission measurement of the microring device**. **a**, Transmission of the microring measured with tunable lasers covering wavelength ranges from 1415 nm to 1480 nm and 1520 nm to 1570 nm. **b**, Normalized transmission scan of the resonance around 1550 nm at a low power (0.1 mW, showing a very slight thermal triangle) and high power (16 mW, showing a very strong thermal triangle). **c**, Transmission of the microring measured with tunable lasers (blue lines) from 939 nm to 955 nm and 962 nm to 990 nm. The resonances in the wavelength gap (purple line) are measured by a third tunable laser covering wavelength range from 915 nm to 985 nm. **d**, Normalized transmission scan of the 978 nm resonance (power = 0.1 mW) when the polarization is TE (blue) and slightly away from TE (red).

III. TRANSMISSION MEASUREMENTS

To characterize the resonances of the microring device in the 1550 nm band, two tunable lasers covering wavelength ranges from 1415 nm to 1480 nm and 1520 nm to 1570 nm are employed. Figure S5a shows the measured transmission (defined as the power collected by the lens fiber from the waveguide output normalized by the power sent to the lens fiber that couples to the waveguide input). As can be seen, even though the microring is multimode, only the fundamental TE mode is observed in the transmission spectrum, thanks to the pulley coupling design[12]. Figure S5b shows the transmission scan of the resonance around 1550 nm. At low powers, the resonance shape is close to Lorentzian; as the power increases, thermo-optic dispersion quickly results in the swept-wavelength lineshape following the commonly observed thermal triangle.

Figure S5c shows the transmission of the 980 nm band, whose characterization involves three tunable lasers. The first two lasers, which have been used as the signal in the downconversion experiment (Fig. 6a in the main paper), cover wavelength ranges from 930 nm to 955 nm and 960 nm to 990 nm. The third laser, which has been used as the 980 nm pump for the wideband conversion experiment, has a tunable wavelength range from 915 nm to 985 nm and a relatively large output power ($\approx$ 45 mW). Considering $\approx$ 6.5 dB coupling loss at the input facet, the maximum on-chip pump power is limited to $<$ 10 mW. Similar to the 1550 nm spectrum, the transmission of the 980 nm band shows that only the fundamental TE mode is well-coupled while other modes are suppressed. However, as illustrated by Fig. S5d, the fundamental TE mode can interact with some other mode at certain wavelengths, which shifts its resonance frequency as shown in Fig. 2f in the main paper. By changing the polarization state of the input light, we find we can increase the extinction ratio of the mode that couples to the TE resonance, suggesting this mode has a different polarization. Through a careful phase-matching analysis, we believe the mode is most likely to be the fundamental TM mode. Such excitation is possible because the TE waveguide mode has a nonzero field overlap with the TM mode of the resonator, though generally the coupling is weak and only strong at certain wavelengths due to an accidental phase matching.

IV. 1550 NM TO 980 NM UPCONVERSION: ADDITIONAL DISCUSSIONS

The experimental setup for the 1550 nm to 980 nm upconversion is shown in Fig. S6a, where a 1550 nm laser is amplified by the EDFA (pump), combined with another 1550 nm laser (signal), and then combined with the 980 nm pump before being coupled to the frequency conversion chip. Figure S6b shows some representative OSA spectra in the 980 nm band as we vary the spectral separation between the signal and the 1550 nm pump, while keeping the pump configuration the same as the example shown in Fig. 5b in the main paper (which

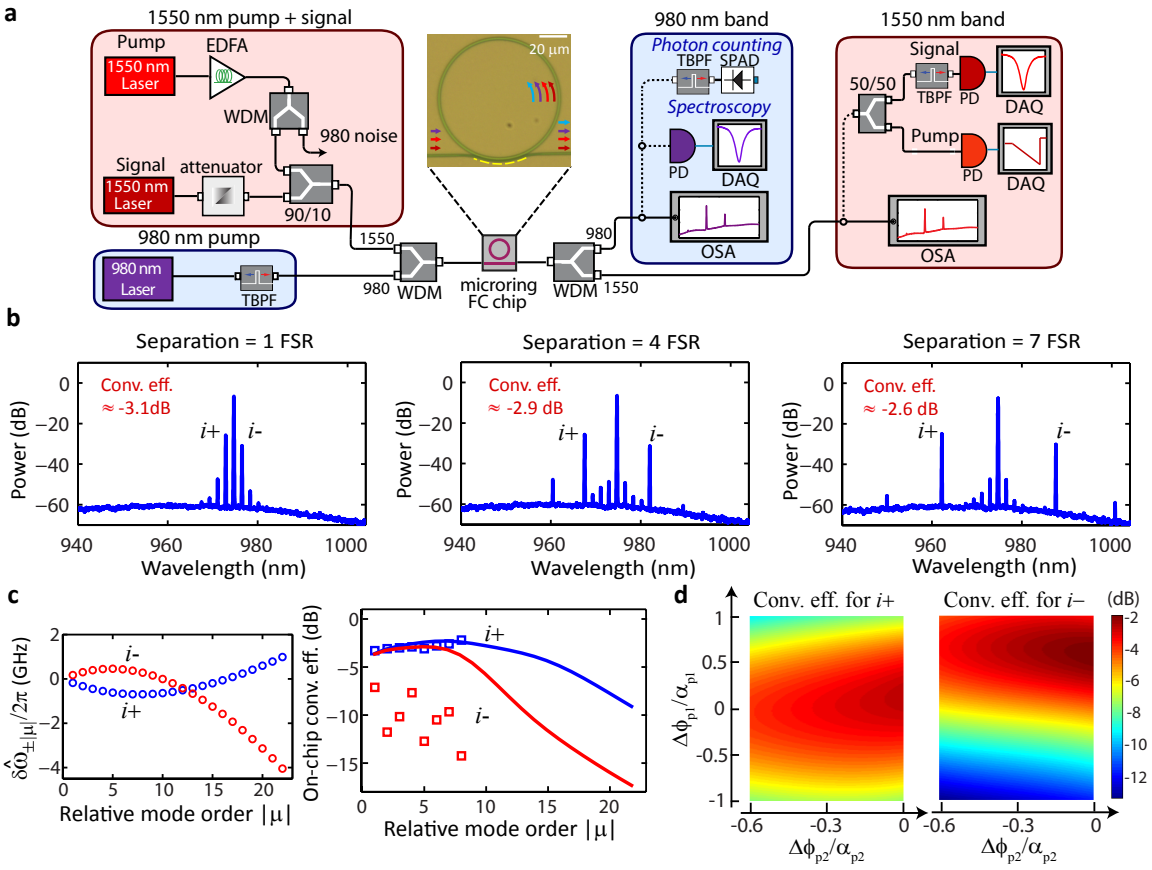


FIG. S6: **Experimental setup and additional data for upconversion**. **a**, Experimental setup for the frequency upconversion from the 1550 nm band to the 980 nm band. **b**, Representative 980 nm OSA spectra of upconversion for different frequency separations between the signal and the 1550 nm pump while keeping the pump configuration fixed: the two pumps in the 980 nm and 1550 nm bands are located at 974.4 nm (power ≈ 8 mW) and 1564.5 nm (power ≈ 50 mW), respectively. A power of 0 dB is referenced to 1 mW. **c**, The left figure shows the calculated frequency detunings for $i+$ and $i-$ at different idler positions, and the right figure compares the measured (markers) and simulated (solid lines) on-chip conversion efficiencies for $i+$ and $i-$ as we vary the separation between the signal and the 1550 nm pump. The error bars for the measured conversion efficiencies due to estimation uncertainties are less than the marker size. In the simulation, $\Delta\phi_{p1}/\alpha_{p1} = 0$ and $\Delta\phi_{p2}/\alpha_{p2} = -0.1$, where α_{p1} and α_{p2} are the cavity loss parameters for the 980 nm and 1550 nm pump, respectively. **d**, Simulated conversion efficiency for $i+$ (left) and $i-$ (right) as a function of the two pump detunings, $\Delta\phi_{p1}$ (980 nm pump) and $\Delta\phi_{p2}$ (1550 nm pump).

corresponds to 8 FSR separation). By examining Eq. S30 (effective detuning of $i+$ in upconversion) and Eq. S33 (effective detuning of $i+$ in downconversion), we find the frequency detuning of $i+$ is essentially the same for the upconversion and downconversion schemes (except that the sign is opposite), suggesting similar performance for $i+$ between the two cases in terms of conversion efficiency and bandwidth. This is confirmed by comparing the experimental data to the simulation results based on the coupled mode equations as discussed in Section I.B (Fig. S6c). On the other hand, the frequency detuning for $i-$ (Eq. S31) is significantly different from the downconversion case (Eq. S34), which seems to indicate that $i-$ should have similar conversion efficiencies as $i+$ even for reasonably large $|\mu|$ values. However, the measured conversion efficiencies are much worse than the simulation results (Fig. S6c). The discrepancy can be attributed to several factors. First, some resonances accommodating $i-$ have been shifted in the spectrum by mode interactions (such as $\mu = -2, -3$, see Fig. 2f in the main paper), which cause large frequency detunings that are not accounted for in the simulation. Second, the transmission at certain resonances (such as $\mu = -8$, see Fig. S5c) is much worse than other resonances, possibly due to some resonant scattering from defects along the waveguide or on the cleaved facets, leading to less power in the transmitted idlers. Finally, the frequency detuning of the two pumps can drift during the experiment, which impacts the two idlers in a different way. The 1550 nm pump is always blue detuned (i.e., $\Delta\phi_{p2} < 0$), since otherwise the thermal lock will be lost and no conversion efficiency will be observed. On the other hand, the 980 nm pump exhibits a Lorentzian transmission scan due to the fact that its power is much smaller compared to the 1550 nm pump. Though in the experiment we try to set $\Delta\phi_{p1} \approx 0$ by parking the laser to its minimum of transmission, it has been observed that the 980 nm pump can often drift away from the initial position within a relatively short time. As can be seen from the simulation shown in Fig. S6d, $i-$ is much more sensitive to the pump detunings than $i+$ for the device under study, especially to the detuning of the 980 nm pump.

V. 980 NM TO 1550 NM DOWNCONVERSION: ADDITIONAL DISCUSSIONS

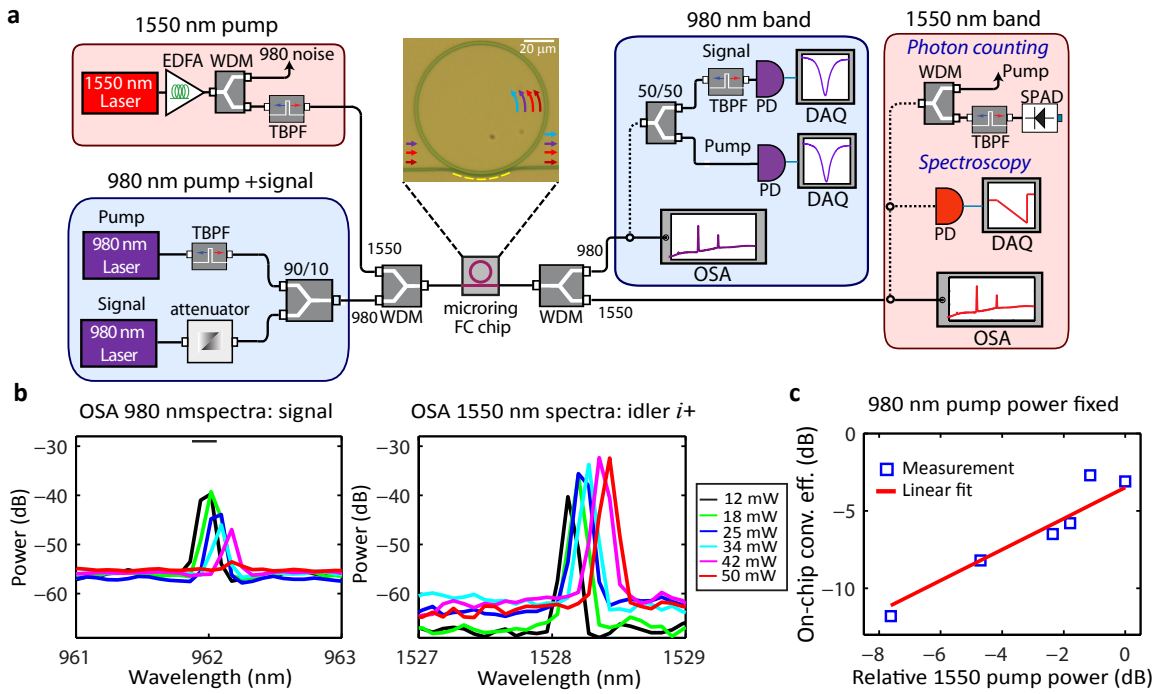


FIG. S7: **Experimental setup and additional data for downconversion**. **a**, Experimental setup for the frequency downconversion from the 980 nm band to the 1550 nm band. **b**, Superimposed OSA spectra for the 980 nm signal (left) and the 1550 nm idler $i+$ (right) corresponding to various 1550 nm pump powers (located at 1559.8 nm) and a fixed 980 nm pump power around 8 mW (located at 974.4 nm). The small horizontal bar in the left figure marks the signal off-resonance power (≈ -29 dB), where a power of 0 dB is referenced to 1 mW. **c**, Extracted conversion efficiencies for $i+$ from **b** (markers) plotted against a linear fit (solid line), showing that the conversion efficiency is proportional to the 1550 nm pump power. The error bars for the measured conversion efficiencies due to estimation uncertainties are less than the marker size. A power of 0 dB in the x axis is referenced to the maximum power used in the experiment (50 mW).

The experimental setup for the 980 nm to 1550 nm downconversion is shown in Fig. S7a, where we have added a narrowband filter (bandwidth $\approx$ 100 GHz) after the EDFA to remove the ASE noise. In addition, cascaded WDM filters have been used at the detection side to reject the 1550 nm pump ($>$ 120 dB suppression) while allowing idlers to pass with a small insertion loss ($\approx$ 3 dB). The transmitted idlers are bandpassed by a narrowband filter with a tunable bandwidth (32 pm to 600 pm, , see Fig. S8b for its transmission response) and center wavelength (1460 nm to 1560 nm) before detection by a SPAD. Figure S7 shows the OSA spectra by varying the 1550 nm pump power while keeping the 980 pump power fixed. (The pump and signal configuration is the same as the example shown in Fig. 5d in the main paper.) As can be seen, the extinction ratio of the signal resonance increases with the 1550 nm pump power (left figure), while the generated idler $i+$ increases initially and then saturates (right figure). The summarized conversion efficiency of $i+$ versus the 1550 nm pump power shown in Fig. S7c indicates the conversion efficiency scales linearly with the 1550 nm pump power, which is expected as the the conversion efficiency is determined by the product of two pump powers (see Eq. S37)[13].

VI. BACKGROUND NOISE MEASUREMENTS

In this section, we provide additional data on the background noise measurements performed in this work. Figure S8a shows the measured transmission response (blue curve) of the tunable bandpass filter used in the noise measurement for the 980 nm intraband conversion (Fig. 4e in the main paper), which consists of a 980 nm bandpass filter with a tunable center wavelength from 970 nm to 990 nm and a fixed bandwidth of 0.4 nm, and a longpass filter which suppresses light below 930 nm ($\approx$ 1 dB insertion loss to light with wavelengths $>$ 930 nm). It is found that when the 1550 nm pumps are on resonance, the measured noise by the SPAD can increase significantly (more than tenfold increase) if we remove the 930 nm longpass filter, indicating the majority of the noise is below the wavelength of 930 nm. Inspecting the 980 nm bandpass filter with a supercontinuum white light source and an OSA reveals that the bandpass filter has a wide passband below 820 nm (red curve in Fig. S8a), suggesting the excessive noise (without the 930 nm longpass) is likely to have wavelengths below 820 nm. The investigation of its exact nature is the subject of future study.

Figure S8b shows the transmission responses of the narrowband filter used for the noise measurement in the frequency downconversion experiment (Figs. 6c and 6d in the main paper), which is used to bandpass filter the downconverted idler in the 1550 nm band before the

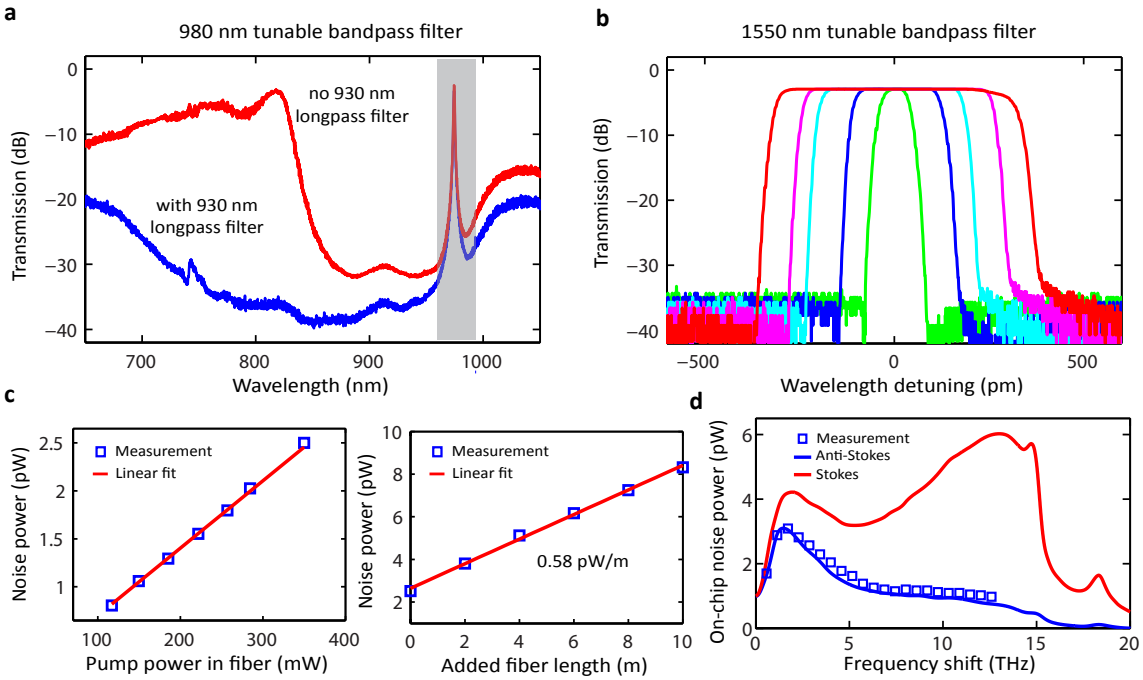


FIG. S8: **Filter responses and additional data on background noise measurement**. **a**, Filter response of the tunable bandpass filter used for the background noise measurement in the 980 nm intraband conversion experiment (Fig. 4e in the main paper). The passband that is used for the selection of the idler is highlighted. The blue and red curve corresponds to the response of the filter with and without a 930 nm longpass filter, respectively. **b**, Representative filter responses of the bandpass filter used for the background noise measurement in the downconversion experiment (Figs. 6c and 6d in the main paper), showing that its bandwidth can be tuned from 80 pm to 600 pm with almost the same insertion loss. **c**, Background noise measured at the output of the narrowband filter after the EDFA at the input side (see Fig. S7a) as a function of the pump power in the fiber (left) and added fiber length for a fixed pump power around 350 mW in the fiber (right). On the detection side, the bandpass filter is set at 1528 nm (pump located at 1559.8 nm) with a filtering bandwidth of 80 GHz for both cases. **d**, The markers are the measured on-chip noise when the 1550 nm pump is off resonance for a detection bandwidth of 80 GHz (data re-plotted from Fig. 6c in the main paper as a function of the frequency shift from the pump), while the solid lines are the spontaneous Raman noise spectra from fibers for Stokes (red) and anti-Stokes (blue) sidebands [6,8,14]. The error bars in **c**-**d** are smaller than the marker size.

detection by a SPAD. The filter has a tunable bandwidth of 32 pm to 600 pm (although below 80 pm the insertion loss starts to increase), and a tunable center wavelength from 1460 nm to 1560 nm. As mentioned in the main paper, when the 1550 nm pump is off resonance, we find a broadband noise that scales with the detection bandwidth and is linearly dependent on the pump power. Moreover, the measured noise is almost the same if we remove the chip and introduce a similar insertion loss between the two lensed fibers, strongly suggesting the noise is from the fiber itself. Figure S8c measures the noise at a fixed frequency shift (≈ 4 THz) from the pump at the input side (no chip), showing that the measured noise is linearly proportional to the pump power in the fiber (left figure) and increased fiber length for a fixed pump power (right figure). The extracted ratio of the increased noise power with the fiber length (≈ 0.58 pW/m) is consistent with the anti-Stokes Raman signal for a pump power of 350 mW with a detection bandwidth of 80 GHz [6]. To further support this argument, we re-plot the pump-off-resonance noise shown in Fig. 6c in the main paper in Fig. S8d (markers) as a function of the frequency shift, and compare it to the spontaneous anti-Stokes Raman spectrum (blue line, multiplied by a factor to match its peak power to that of the pump-off-resonance noise). The excellent agreement of the spectral shape confirms that the pump-off-resonance noise is mostly likely the anti-Stokes Raman signal generated inside the fiber.

* Electronic address: qing.li@nist.gov
† Electronic address: kartik.srinivasan@nist.gov

1 S. Coen, H. G. Randle, T. Sylvestre, and M. Erkintalo, "Modeling of octave-spanning Kerr frequency combs using a generalized mean-field Lugiato–Lefever model," Optics Letters **38**, 37–39 (2013).
2 Y. K. Chembo and N. Yu, "Modal expansion approach to optical-frequency-comb generation with monolithic whispering-gallery-mode resonators," Physical Review A **82**, 033 801 (2010).
3 T. Hansson, D. Modotto, and S. Wabnitz, "On the numerical simulation of Kerr frequency combs using coupled mode equations," Optics Communications **312**, 134–136 (2013).
4 Y. K. Chembo and C. R. Menyuk, "Spatiotemporal Lugiato-Lefever formalism for Kerr-comb generation in whispering-gallery-mode

resonators," Physical Review A **87**, 053 852 (2013).
[5] Y. Huang, V. Velev, and P. Kumar, "Quantum frequency conversion in nonlinear microcavities," Optics Letters **38**, 2119–2121 (2013).
[6] G. P. Agrawal, *Nonlinear Fiber Optics* (Academic Press, Amsterdam, 2007).
[7] Q. Lin, T. J. Johnson, R. Perahia, C. P. Michael, and O. J. Painter, "A proposal for highly tunable optical parameteric oscillation in silicon micro-resonators," Optics Express **16**, 10 596–10 610 (2008).
[8] W. C. Jiang, X. Lu, J. Zhang, O. J. Painter, and Q. Lin, "Silicon-chip source of bright photon pairs," Optics Express **23**, 20 884–20 904 (2015).
[9] X. Zeng and M. A. Popovic, "Design of triply-resonant microphotonic parametric oscillators based on Kerr nonlinearity," Optics Express **22**, 15 837–15 867 (2014).
[10] H. A. Haus, *Waves and Fields in Optoelectronics* (Prentice-Hall, Englewood Cliffs, New Jersey, 1984), 1st edn.
[11] Q. Lin, O. J. Painter, and G. P. Agrawal, "Nonlinear optical phenomena in silicon waveguides: modeling and applications," Optics Express **15**, 16 604 (2007).
[12] E. Shah Hosseini, S. Yegnanarayanan, A. H. Atabaki, M. Soltani, and A. Adibi, "Systematic design and fabrication of high-Q single-mode pulley-coupled planar silicon nitride microdisk resonators at visible wavelengths," Optics Express **18**, 2127–2136 (2010).
[13] I. Agha, S. Ates, M. Davanço, and K. Srinivasan, "A chip-scale, telecommunications-band frequency conversion interface for quantum emitters," Optics Express **21**, 21 628–21 638 (2013).
[14] Q. Lin, F. Yaman, and G. P. Agrawal, "Photon-pair generation in optical fibers through four-wave mixing: Role of Raman scattering and pump polarization," Physical Review A **75**, 023 803 (2007).